Science & Technology Facilities Council

Technical Report
RAL-TR-2013-008

Monte Carlo modelling of the OSIRIS neutron backscattering spectrometer

K Pokhilchuk

July 2013

RAL Library
STFC Rutherford Appleton Laboratory
R61
Harwell Oxford
Didcot
OX11 0QX

Tel: +44(0)1235 445384
Fax: +44(0)1235 446403
email: libraryral@stfc.ac.uk

Science and Technology Facilities Council reports are available online at: http://epubs.stfc.ac.uk

ISSN 1358- 6254

Monte Carlo modelling of the OSIRIS neutron backscattering spectrometer

Konstantin Pokhilchuk

2012-2013

Contents

1. Abstract

This report focuses on modelling the OSIRIS neutron-backscattering instrument using Monte Carlo methods with the use of the McStas software package. The aim is to match the experimental energy resolution of OSIRIS and thus be able to simulate the instrument in order to investigate its various properties and performance characteristics. Furthermore, understanding quantitatively how different components of OSIRIS contribute towards its resolution function will provide insight into potential upgrade possibilities of the instrument. The simulated energy resolution FWHM values of 23.7 μeV for PG002 and 96.3 μeV for PG004 show a good agreement with the experimental results of 25.0 μeV for PG002 and 99.5 μeV for PG004 and are only 5% and 3% lower respectively.

2. Introduction to neutron scattering

Neutron scattering is the art of measuring atomic and magnetic distributions and motions of atoms. In any scattering experiment one measures the properties of the incident and final neutron beams to measure momentum and energy transferred to the sample governed via the following two equations known as the momentum and energy conservations equations (1):

$$Q = k_i - k_f$$

$$\hbar\omega = E_i - E_f$$

where

$$E = \frac{\hbar^2 k^2}{2m_n}$$

The two main types of neutron scattering are elastic and inelastic. Inelastic scattering (also known as spectroscopy) is used to measure the change in energy of neutrons as they scatter from a sample. Spectroscopy is mostly appropriate for studying molecular, magnetic or other excitation processes. Elastic scattering (also known as diffraction) on the other hand is a special case of scattering where kinetic energy of incident neutrons is not changed but only the direction of propagation changes (2).

One possibility for analysing the energy of neutrons is by means of Bragg-scattering from a large array of crystals. Only the neutrons of appropriate energy/wavelength, satisfying the Bragg condition of the crystals, are scattered. Through recording the TOF (time-of-flight) of each neutron a second possibility exists to measure the energy of a neutron. The energy and momentum equations for a neutron are defined as follows (3):

$$E = \frac{1}{2} m_n v^2$$

$$p = m_n v = \frac{h}{\lambda}$$

where m_n is the mass of the neutron. Bragg's law states (3):

$$\lambda = 2d \sin\theta$$

These equations can be re-formulated to yield:

$$E = \frac{1}{2} m_n \left(\frac{L}{t}\right)^2 = \frac{1}{2} m_n v^2 = \frac{p^2}{2m_n} = \frac{1}{2m_n}\left(\frac{h}{\lambda_a}\right)^2 = \frac{1}{2m_n}\left(\frac{h}{2d_a \sin\theta}\right)^2$$

Where L is the flight path, t is the time-of-flight and d_a is the d-spacing of an analyser crystal. If neutron interacts with the sample a loss or gain in energy can occur and then a distribution of arrival times will result. This energy exchange within the sample can be determined by measuring the total time-of-flight, $t = t_1 + t_2$ and by knowing t_2, L_1 and L_2 (3):

$$\Delta E = E_1 - E_2 = \frac{1}{2} m_n \left[\left(\frac{L_1}{(t - t_2)}\right)^2 - \left(\frac{L_2}{t_2}\right)^2\right]$$

There exist two types of TOF spectrometers: utilising either direct scattering geometry, where the initial energy of the neutrons incident on the sample, E_i, is selected by monochromators and/or choppers, or inverted scattering (backscattering) geometry, where the final energy of the neutrons E_f is selected by an analyser crystal. The later setup is known as "near-backscattering", when the Bragg reflection angle is near 90°. This geometry has the advantage of maximising energy resolution of the analyser, making it suitable for analysing and resolving small energy changes (4).

3. Introduction to Monte Carlo

Monte Carlo methods have been appreciated as a powerful tool for performing calculations that are normally too complicated for a classical approach and require a great amount of effort to compute. Since 1950s and the appearance of high speed computers, Monte Carlo methods gained an ever increasing amount of attention as they allowed for more precise prediction of physical experiments (5).

Present day neutron scattering instrumentation consists of a series of optical elements that propagate neutrons from a source to a detector. Since neutron spectroscopy is a very low-signal method it is very important to optimise neutron instrumentation. While simpler setups and individual components may be studied analytically, those methods fail when dealing with a whole range of optical components comprising a typical scattering instrument, where each component modifies various parameters of the incoming neutron beam.

This is where statistical sampling becomes important. Monte Carlo is the set of statistical methods utilised for computational modelling of such cases. It is based on a simple idea of probability sampling of the incoming neutron trajectories. Integrating over all neutron trajectories of a given system results in measurable quantities.

The basic principle of Monte Carlo integration is to statistically integrate a given function over some complicated domain, D. Monte Carlo integration picks random points over a simple domain D', which encompasses D. Suppose D is a circle and we desire to evaluate its integral numerically with Monte Carlo. Now suppose D' is a rectangle of dimensions to perfectly fit the circle. Finding the integral of the rectangle is very simple compared to the circle, it's simply equal to l^2. Now suppose we have a source of neutrons located some distance away from our square. Monte Carlo propagates neutrons with the use of random number generators. In our particular case we are interested in propagating neutrons randomly towards the square. This way the total number of neutrons incident on the circle inside our square divided by the number of neutron incident on both the circle and the square gives us the ratio of the two integrals. In the ideal case this ratio is equal to πr^2 of the circle to $4r^2$ of the square. The more neutrons our source propagates, the more accurate the statistics of Monte Carlo integration. For complex neutron instruments it is usually necessary to simulate many millions of neutrons to get good statistics at the final detectors.

The mathematical representation of this process is shown below. Monte Carlo picks N randomly distributed points x_1, x_2,...., x_n in a multidimensional volume V to determine the integral of a function f in this volume. The result is defined by (6):

$$\int f dV \approx V\langle f\rangle \pm V\sqrt{\frac{\langle f^2\rangle-\langle f\rangle^2}{N}},$$

where

$$\langle f\rangle \equiv \frac{1}{N}\sum_{i=1}^{N} f(x_i)$$

$$\langle f^2\rangle \equiv \frac{1}{N}\sum_{i=1}^{N} f^2(x_i)$$

3.1. McStas

McStas is a software package designed to carry out Monte Carlo ray-tracing simulations of neutron scattering instruments of high complexity. McStas is available for Windows, Macintosh, and UNIX/Linux systems. MatLab was used in conjunction for analysing the instrument geometry. McStas can be used to evaluate and optimize performance of existing equipment, aid design of new instrumentation or to

perform virtual experiments for learning purposes. The software package was originally developed in 1997 at Risø, Denmark, and was later picked up by other institutions such as ILL in France. It consists largely of a library of components, maintained by its user community. Each component is programmed in C++ and serves the purpose of emulating a corresponding physical component, all of which makes up a neutron scattering instrument. Well-known examples of this include components such as moderators, guides, choppers, samples, analyser crystals, detectors. The user may then construct a desired instrument by modelling those components in McStas's own meta-language C++ editor. Version 1.12c (2011) of the software was used throughout this report.

3.2.Neutron weight and importance sampling

McStas is designed with speed in mind and utilises a notion known as neutron "weight factor". It works by adjusting the weight of each simulated neutron according to its probability propagating through some path. Suppose that a certain component has a reflectivity equal to 10 %. In a realistic scenario each of the neutron rays has to be processed, including the 90 % that don't reflect off the component, only to be discarded. This wastes computational power on the rays that never pass the component and are thus of no importance. A much better approach is to make each of the simulated rays pass the component but multiply their neutron weight by 0.1 to adjust the integrated intensity value for the component's reflectivity factor. Thus only one ray needs to be simulated to pass the component, instead of an average of ten rays. The weight factor for a neutron ray after passing the whole instrument is a product of all contributions, as described by P. Willendrup et al (7) in the following equation:

$$p = p_n = p_0 \prod_{j=1}^{n} \pi_j$$

where p_0 is the initial neutron weight, and π_j is the weight multiplication factor in the j^{th} component. Importance sampling is another technique of optimising speed of simulations by discarding neutron rays that are very unlikely to arrive at a desired point, i.e. neutrons that don't initially enter a guide that focuses on a sample, and hence are extremely unlikely to hit the sample. To account for this, many of the components that scatter neutrons such as moderators and samples have the option of specifying a solid angle of focus to scatter neutron into a certain direction.

3.3.Statistics and errors

The result of any Monte Carlo simulation consists of integrating neutron rays of different weights. The sum of these weights is an estimate of the mean number of neutrons hitting a monitor per second:

$$I = \sum_i p_i = N\bar{p}$$

where N is the number of rays hitting a detector and $\bar{p}$ bar represents the average probability of interaction. The mean value of I is unchanged by performing weight transformations while N will in general increase. The general equation representing statistical uncertainty of the observed intensity for large numbers is (7):

$$\sigma(I) = \sqrt{N}\bar{p} = \frac{I}{\sqrt{N}}$$

where σ(I) is the variance of the intensity.

3.4. McStas detector/monitor parameters

Intensity: Average number of neutron rays detected by a monitor per channel
I: Total integrated neutron intensity
Err: Error of the integral
N: Total number of neutrons detected by a monitor
X0: X-value at maximum intensity (peak value)

3.5.Introduction to OSIRIS

OSIRIS is a high–resolution time-of-flight neutron backscattering instrument located at ISIS, Rutherford Appleton Laboratory. It is optimised for very low energy studies and long wavelength diffraction. It may be used either as a high-resolution long wavelength diffractometer or a high-resolution quasi/inelastic neutron spectrometer. The geometry of OSIRIS is optimised for high-flux spectroscopy owing to its super-mirror guides. Incoming neutrons travel from the liquid hydrogen moderator through the guide and to the sample. Those neutrons are then scattered off the sample into the bank of PG analyser crystals, and backscattered under Bragg condition into the detector bank. The scattered patterns on the detectors are representative of the sample used and allow for a study its excitations and slow diffusive motions of atoms (8) (9).

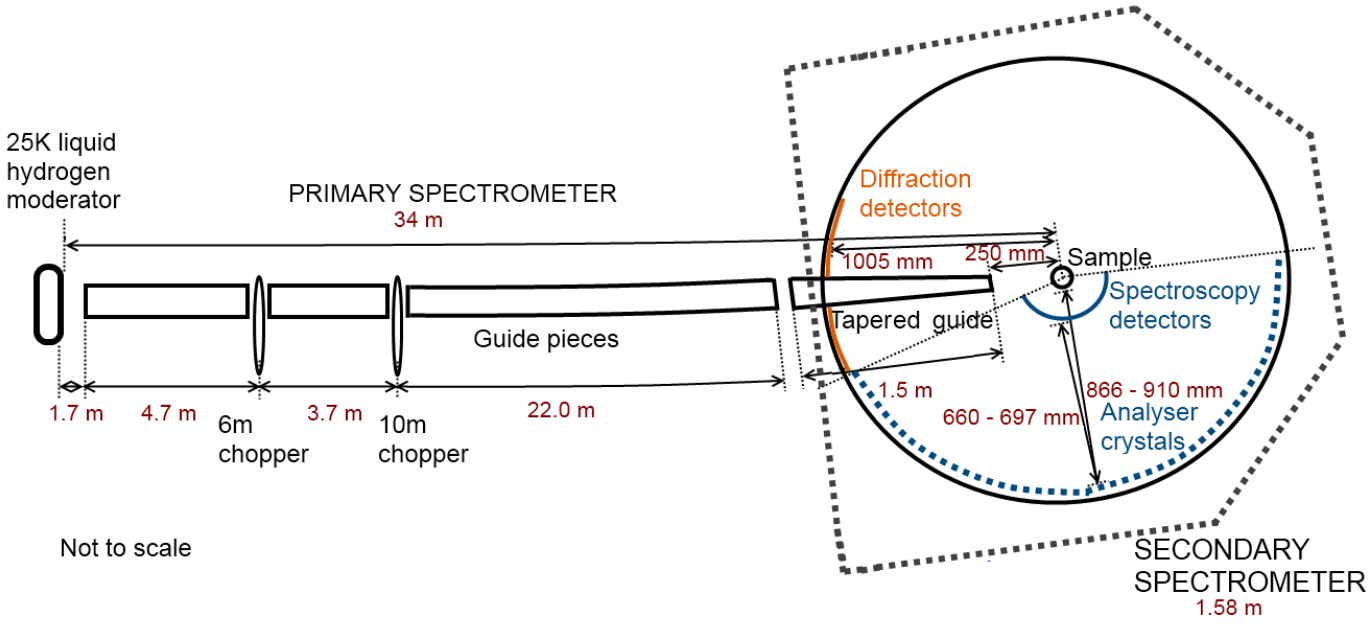

Figure 1: Top view of the OSIRIS instrument.

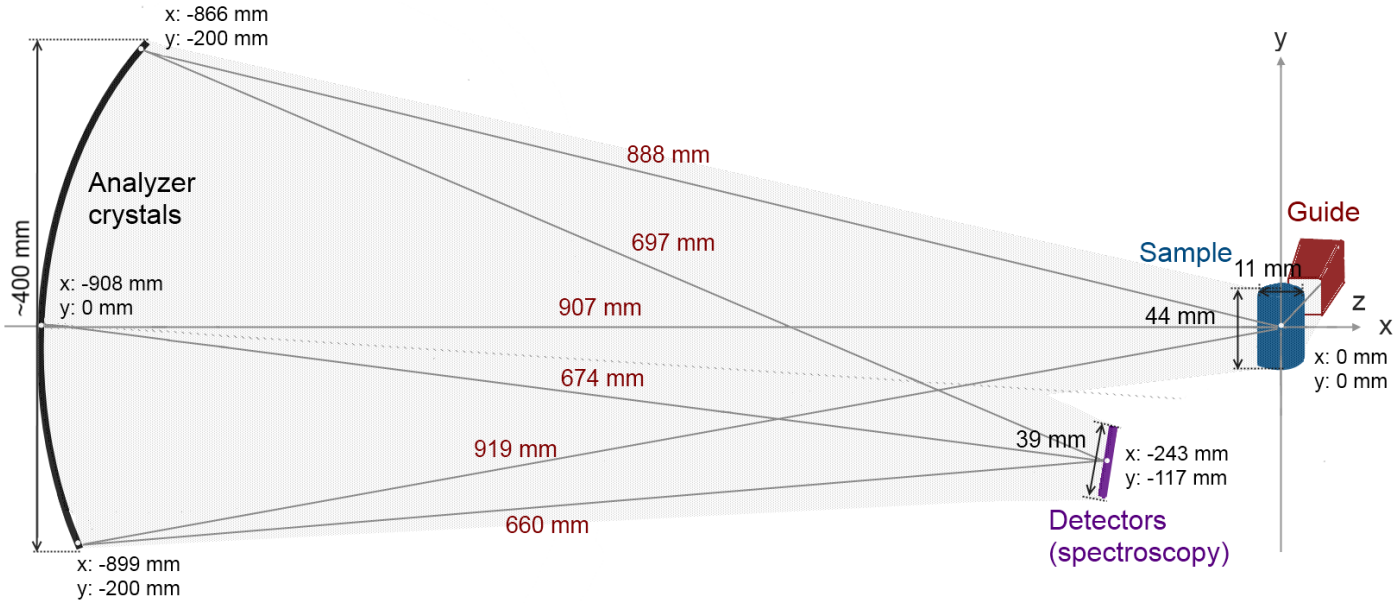

Figure 2: Side view of the OSIRIS secondary spectrometer. Secondary flight path is approximately 1.58m.

The graph below shows a neutron intensity distribution over wavelength for OSIRIS, IRIS and HRPD instruments. Note a significant increase in neutron flux of OSIRIS compared to IRIS. This is due to the use of a supermirror guide on OSIRIS, compared to nickel-plated glass tubes used on IRIS (10).

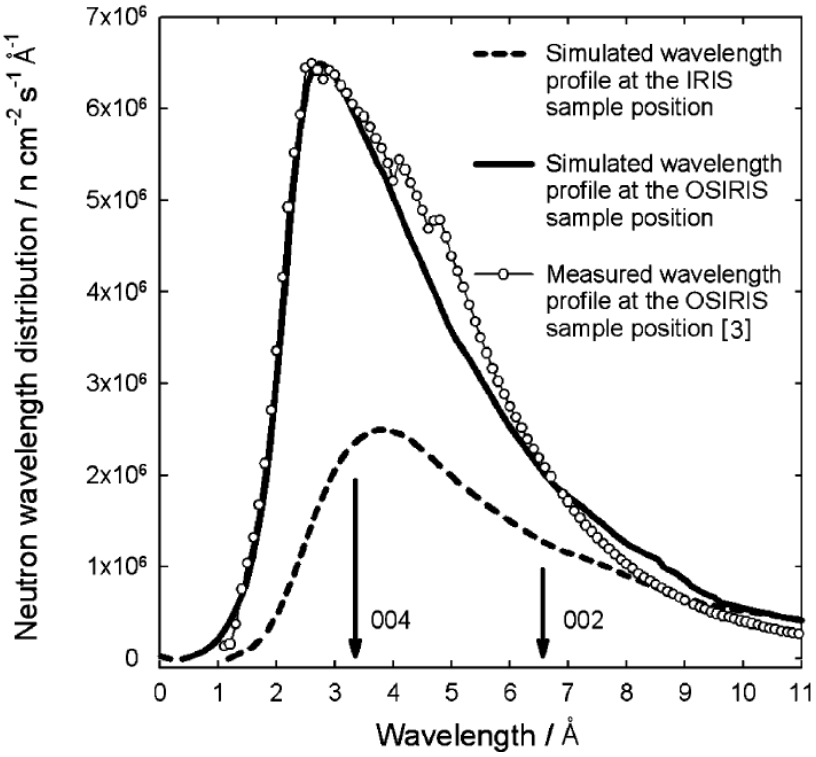

Figure 3: Wavelength distributions at the OSIRIS sample position. Simulated results are from a different report. (8)

The secondary spectrometer consists of a vessel of 2m in diameter. The most prominent features of the secondary spectrometer are the sample (located roughly at the centre of the vessel), an array of radial collimators (to prevent detector signal cross-contamination), a pyrolytic analyser array (known as monochromators, the components that Bragg-analyse the incoming neutron signal). The analyser array reflects neutrons slightly below the sample, where the spectroscopy detector assembly is present. The graphite analyser bank is cooled to a low temperature of approximately 8K to minimize background contributions from thermal diffuse scattering. Also, parameters of the incoming beam are monitored with the use of incoming and transmitted beam monitors.

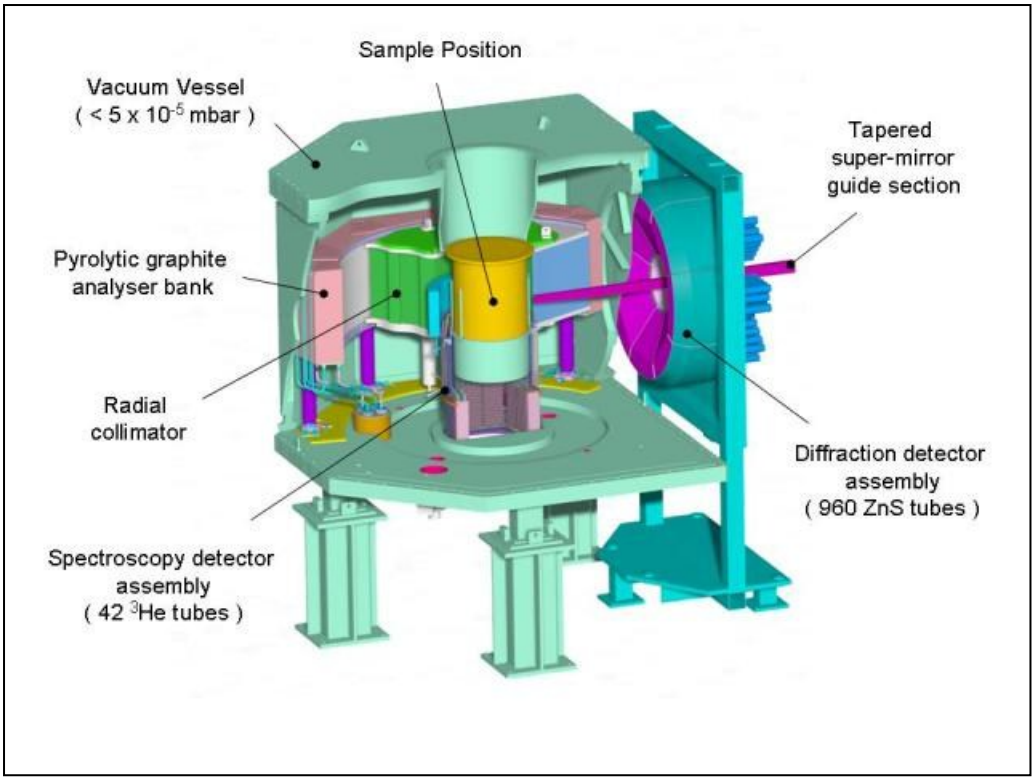

Figure 4: A 3D schematic of the OSIRIS secondary spectrometer (11).

3.6.Previous simulations with VITESS

OSIRIS has previously been modelled with another neutron ray-tracing application known as VITESS (The **V**irtual **I**nstrumentation **T**ool for the **ESS)** and showed good agreement with experimental resolution results. Figure 5: The FWHM value obtained for PG002 through VITESS simulations is only 2% bigger than the experimental value. Note however, that the latest experimental data indicates OSIRIS's energy resolution to be in the range of approximately 25µeV. The experimental data is taken at 8K, the standard temperature range used for OSIRIS experiments. demonstrates that the energy resolution FWHM is almost perfectly matched in VITESS, however the shape of the simulated resolution function is somewhat asymmetric and does not represent the experimental result ideally (8).

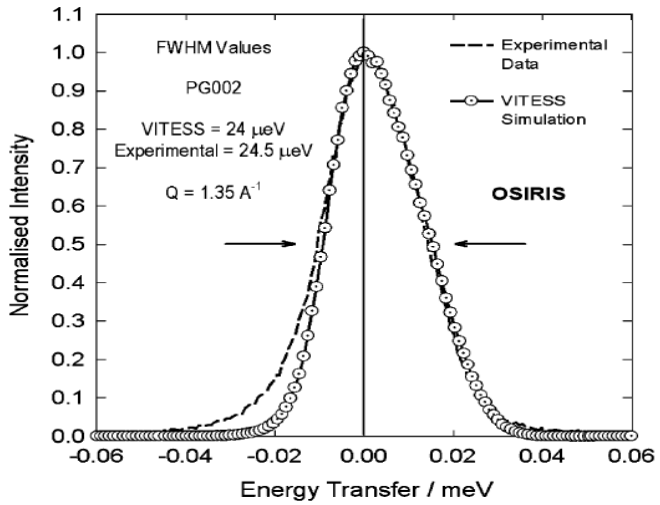

Figure 5: The FWHM value obtained for PG002 through VITESS simulations is only 2% bigger than the experimental value. Note however, that the latest experimental data indicates OSIRIS's energy resolution to be in the range of approximately 25µeV. The experimental data is taken at 8K, the standard temperature range used for OSIRIS experiments.

4. Building the instrument

4.1.Moderator

The moderator used for both OSIRIS and IRIS is a liquid hydrogen tank cooled down to 25K. This provides a large flux of long-wavelength cold neutrons. The McStas component file "h.iris" representing this moderator has previously been modelled by Stuart Ansell (ISIS Facility) using MCNP (**M**onte **C**arlo **N**-**P**article Transport Code) and was used for the purpose of modelling OSIRIS in this report.

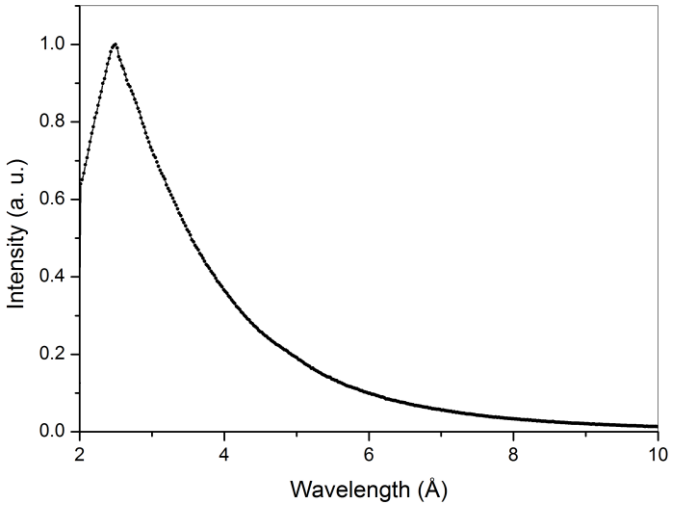

Figure 6: Wavelength distribution of the moderator at the input energy range of 0.8 – 20.5 meV, which corresponds to wavelengths of approximately 2 – 10 Å.

4.1.1. Moderator time-of-flight tests

The purpose of this investigation was to compare experimentally obtained TOF FWHM values of the OSIRIS hydrogen moderator with the corresponding file "h.iris" used for the simulations, primarily at the value of 6.66Å relevant to studying the PG002 peak, but also to perform tests over a range of other values to see how the moderator TOF FWHM values change as a function of wavelength. Figure 7: A schematic of the moderator on the left with monitors shown as squares, moving along to the PSD detector and the first guide piece on the right. illustrates the setup, where a blue rectangle on the left shows TOF and wavelength monitors both placed 1mm away from the moderator, while the square at 1.6m represents a PSD detector and blue lines further to the right represent the first guide piece. The input energy values were adjusted each time to achieve the required input wavelength. The width of the energy input range was kept at 10μeV for each run.

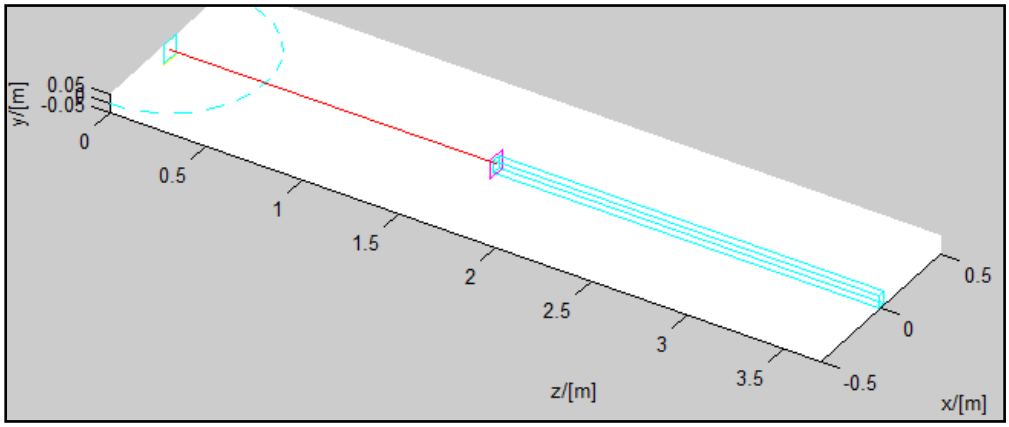

Figure 7: A schematic of the moderator on the left with monitors shown as squares, moving along to the PSD detector and the first guide piece on the right.

λ (Å)	Minimum input energy (meV)	Maximum input energy (meV)	TOF FWHM (µs)
2.00	20.446	20.456	29.4
3.00	9.084	9.094	54.7
4.00	5.108	5.118	71.5
5.00	3.267	3.277	89.7
6.00	2.267	2.277	111.6
6.66	1.835	1.845	114.9
7.00	1.664	1.674	131.2
8.00	1.273	1.283	141.3
9.00	1.005	1.015	150.3
10.00	0.813	0.823	183.4
11.00	0.671	0.681	206.1
12.00	0.563	0.573	201.9
13.00	0.480	0.490	222.7
14.00	0.413	0.423	227.5
17.00	0.280	0.290	273.5
20.00	0.201	0.211	273.5
30.00	0.090	0.100	N/A

Table 1: Test results of the moderator FWHM as a function of wavelength, with energy as the input variable.

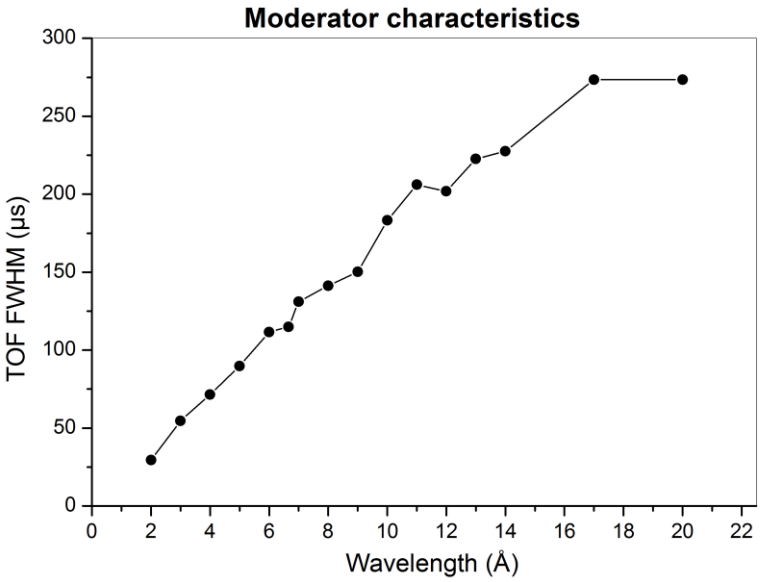

Figure 8: Moderator Time-of-flight FWHM values as a function of wavelength.

The TOF FWHM value of approximately 114 µs obtained through the simulation at the input wavelength value of 6.66Å corresponds well to the previously estimated value of ≈110µs. However, running the tests with wavelengths higher than 20 Å produced TOF curves that contained multiple peaks preventing. At this point the modelled moderator file might hit its limitation.

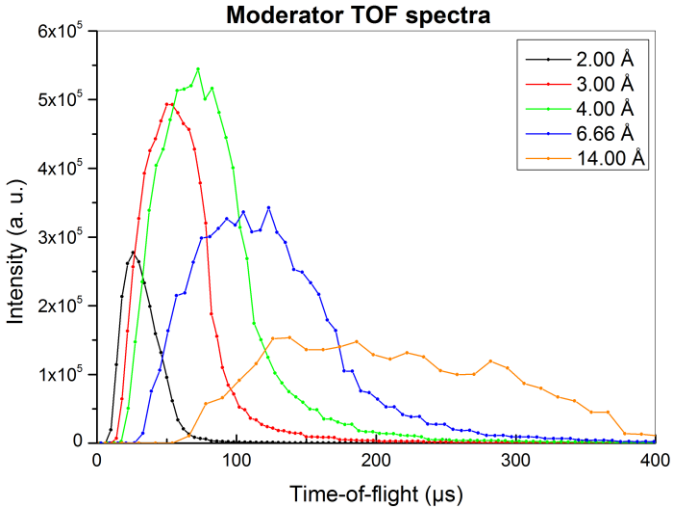

Figure 9: A graph illustrating some of the moderator TOF curves corresponding to a number of input wavelengths.

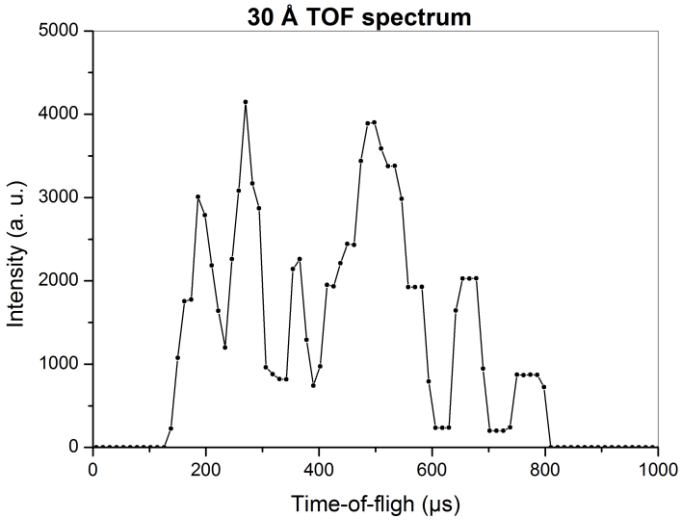

Figure 10: Moderator TOF curve for the 30 Å simulation. As can be seen FWHM is no longer an effective measure of the moderator performance due to multiple peaks.

4.2.Choppers

Choppers are circular components built from neutron absorbing material which contain at least one aperture through which neutrons may pass. When a beam of neutrons is passed through the first chopper it is still considered to be white. By having two choppers separated at a particular distance and rotating at a particular frequency, it is possible to split the continuous incoming neutron beam into pulses. Having both choppers rotating at a specific frequency one has control over the “accepted” time-of-flight range of the incoming neutrons.

OSIRIS has two disc choppers of 30 cm radius used to define the incoming range of neutrons. The first chopper is located approximately 6.3 m away from the moderator and has a 66° wide aperture, while the second one at approximately 10 m with a 98° wide aperture. These choppers can operate at the frequencies of 50, 25, 16.6 or 10 Hz but are synchronised to the ISIS operating frequency of 50Hz (8). The second chopper is used to avoid “frame overlap”, where faster neutrons from historical pulses pass the first chopper at the same time as slower, desired neutrons from subsequent pulses thus making the ray indistinguishable in energy with just one chopper. Thus one can specify the incoming energy or wavelength range incident on the sample.

Chopper time-of-flight and wavelength tests

A number of short tests have been carried out to understand the effect of choppers on the incoming and outgoing wavelength distributions. To is end a total of four time-of-flight and four wavelength monitors were placed, one of each type before and after each of the choppers. Results were plotted to compare performance of the choppers. In McStas there is actually no need to account for frame overlap as McStas simulates everything as a single incoming pulse of neutrons independent of the number of neutrons specified, so the second chopper does not play a big role in simulations. For the 1.2 – 3.5 meV simulated energy range the first chopper filters out approximately 31% of the incoming neutron flux.

Simulated neutron count: 100 million

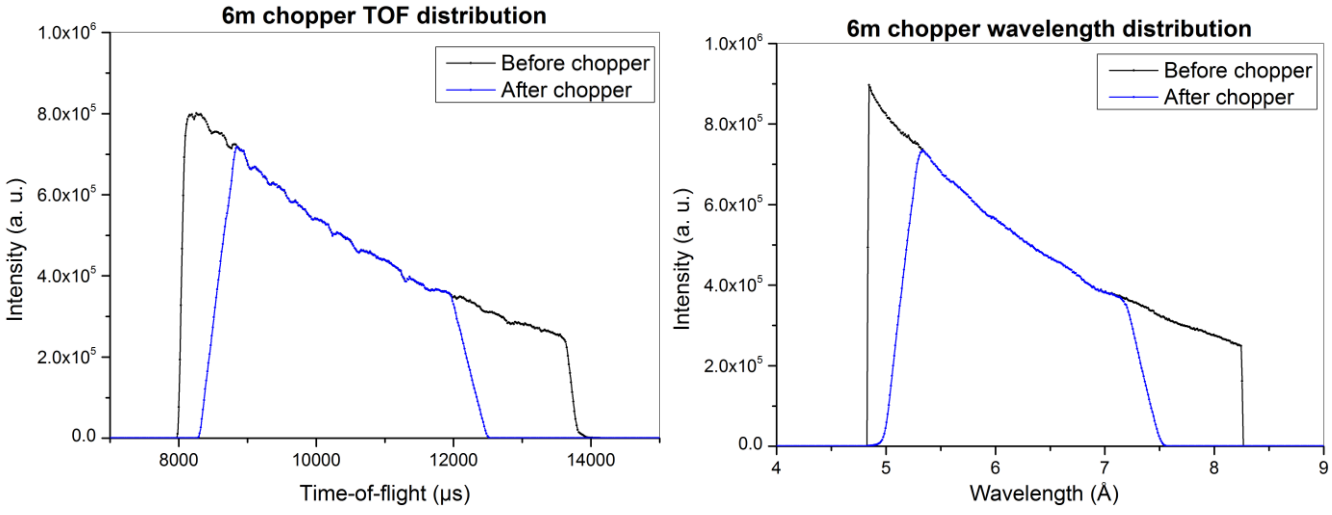

Figure 11: The 6 m chopper time-of-flight and wavelength distribution curves showing how the chopper filters the neutron beam.

4.3.Guide

After neutrons are produced by spallation and moderated down to low energies, they are guided through beam holes in the biological shielding towards the scattering instrumentation. However, the neutron flux falls dramatically with distance travelled. Neutron guides coated with nickel help preserve neutron flux by effectively focusing the beam on the sample. At present, guides of highly reflexing multilayers can be found in many forms for shaping the outgoing beam profile. If the guide is curved the sample can also be protected from unwanted highly energetic neutrons in its direct line of sight as highly energetic neutrons have a greater probability of being absorbed by the guide (12).

OSIRIS has a 32 m long curved guide with a radius of curvature of 2.05 km while the total distance from the moderator to the sample is 34 m. The majority of the guide consists of accurately aligned m=2 supermirror sections approximately 1 m in length, with a 1.5 m converging m=3.5 guide piece at the end (known as the tapered guide section). Entry dimensions of the tapered guide are the same 43 mm wide by 65 mm high, while exit dimensions are 22 mm wide by 44 mm high. Due to the curvature of the guide no neutron with a wavelength less than around 1.5Å is transported. The incident neutron flux at the sample position integrated over all wavelengths is approximately 2.7×10^{7}n $cm^{-2}s^{-1}$ at full ISIS beam intensity (8).

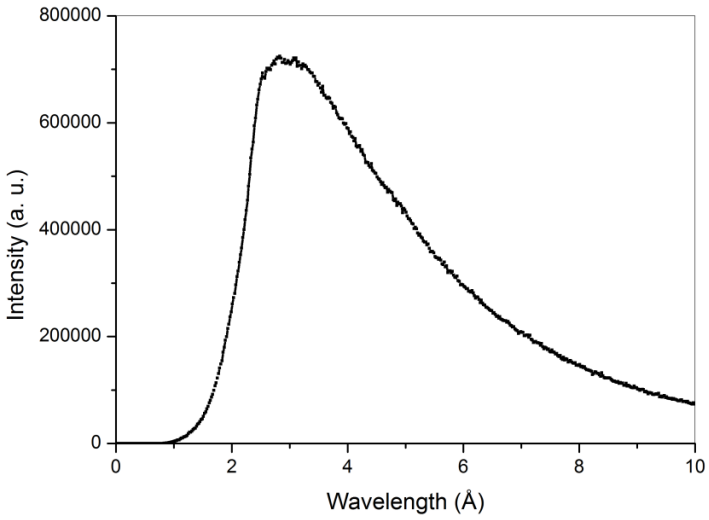

Figure 12: Wavelength distribution after the tapered guide.

4.3.1. Tapered guide neutron position tests

In the following investigation a number of monitors were placed to observe how neutron ray distribution changes with respect to position as neutrons travel through the tapered guide. These monitors were placed just after the second last guide piece and right after the tapered guide piece. Measurements have confirmed the uniformity of the neutron intensity spread to a high degree.

Simulated neutron count: 100 million.

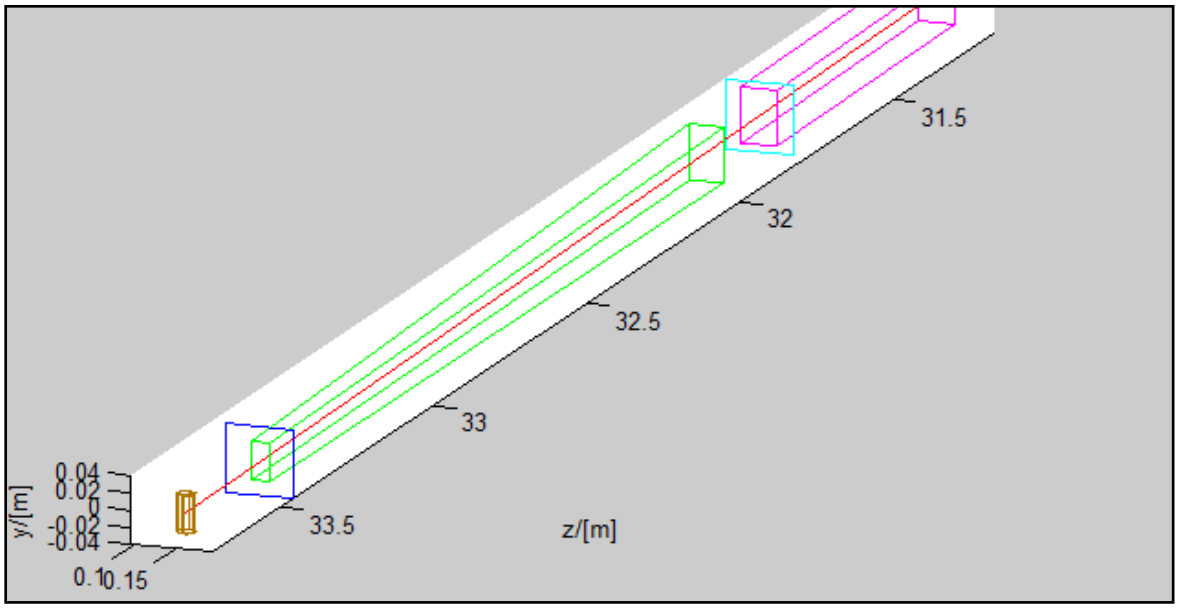

Figure 13: A schematic of the setup showing as two rectangles a PSD detector after the second last guide piece (right), and a PSD detector after the tapered guide (left) and the cylindrical sample.

The following graphs represent 8 x 8 cm PSD monitors before and after the tapered guide. The PSD monitors are colour-coded and are only used for rough evaluation of uniformity of the neutron distribution. As may be observed the colour spread through the monitors is quite consistent, accounting for a gradual fall in intensity towards to positive axis for the curved guide section and almost no difference in distribution for the straight tapered guide.

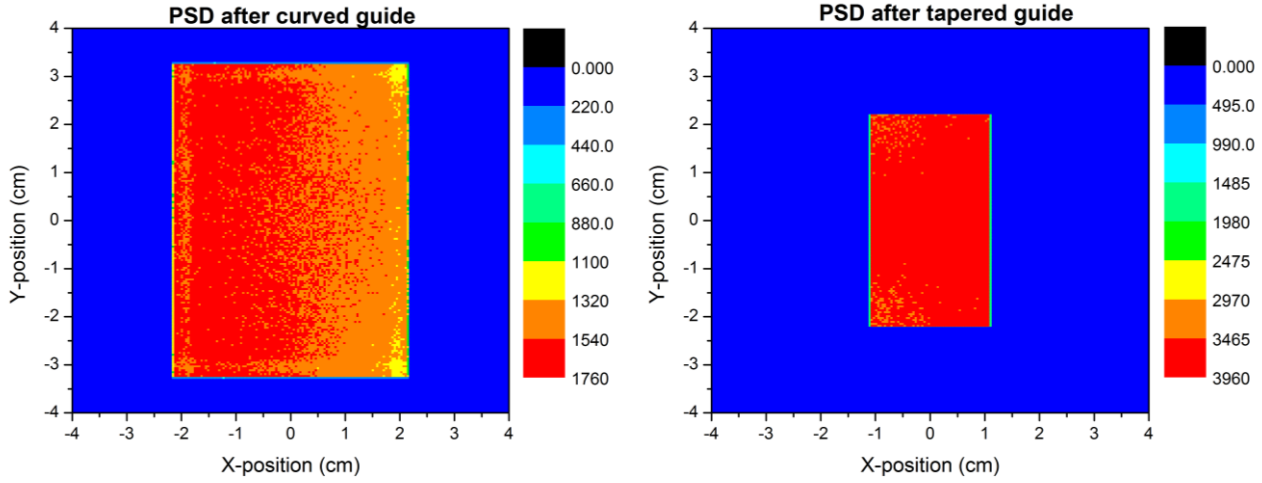

Figure 14: Distribution of neutron intensity before the tapered guide on the left, after on the right.

A much better representation of uniformity is achieved through the use of linear position monitors, which present neutron intensity or as a function of x and y positions independently. The results show symmetric intensity distributions both before and after the tapered guide. The x-position distribution intensity at the end of the tapered guide is as expected slightly asymmetric due to overall curvature of the guide along the x-z plane.

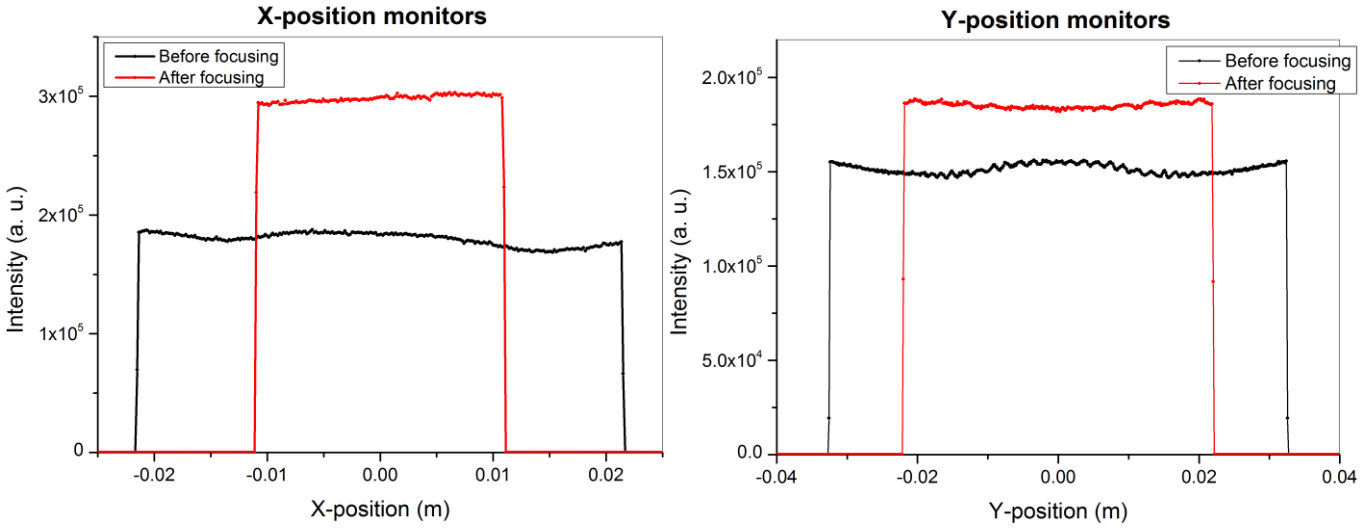

Figure 15: In black the x and y position flux distribution before the tapered guide, in red – after. A narrowing of the neutron signal is evident and corresponds to the narrowing of the tapered guide. Integrated intensity after the tapered guide is slightly lower mostly due to the fact that there is a small gap between the two pieces (they are not joined together). This allows some of the neutrons to escape the boundaries of the tapered guide, and also because some of the neutrons are absorbed in the process of transporting through the tapered guide.

4.3.2. Tapered guide wavelength tests

Two wavelength monitors have been placed one before the tapered guide (at the end of the second last guide piece), and one just after the tapered guide, to measure the loss in neutron intensity as a function of wavelength. The input wavelength was in the range of 2-8 Å. From Figure 16: On the left, incoming intensity before the tapered guide in black, incident intensity after in blue. On the right a divided intensity plot – incoming intensity divided by outgoing intensity. The difference in the ratio of the beams peaks at 18.7% for 5.6 Å and falls to 17.2% at 7.6 Å it can be concluded that the focusing efficiency is slightly higher for colder neutrons.

Simulated neutron count: 1 billion

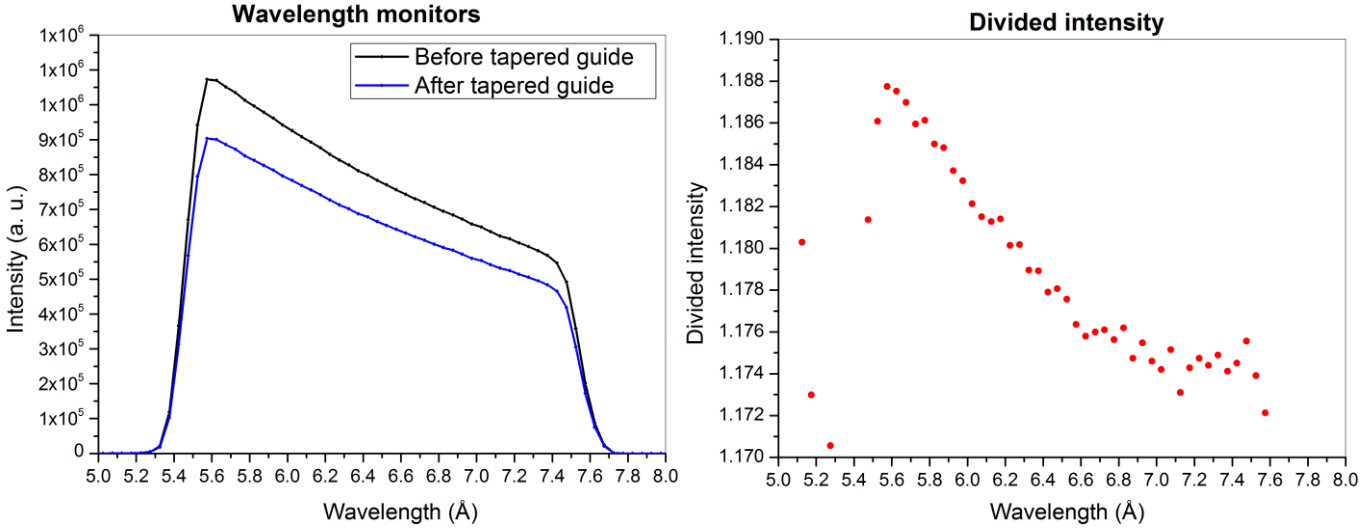

Figure 16: On the left, incoming intensity before the tapered guide in black, incident intensity after in blue. On the right a divided intensity plot – incoming intensity divided by outgoing intensity. The difference in the ratio of the beams peaks at 18.7% for 5.6 Å and falls to 17.2% at 7.6 Å.

4.3.3. Neutron distribution and divergence tests at the sample position

In this test position and divergence distributions of the incoming neutron beam was investigated with the use of PSD and divergence monitors placed just before the sample. The divergence monitor is a two-dimensional monitor that resembles the PSD monitor, but outputs intensity as a function of divergence. It outputs three two-dimensional arrays of counts: $n(\eta_v, \eta_h)$, $I(\eta_v, \eta_h)$, $M_2(\eta_v, \eta_h)$, where η_v is defined as vertical divergence, while η_h as horizontal. Both are defined by the following equations respectively:

$$\eta_v = \tan^{-1}\left(\frac{V_y}{V_z}\right) \quad [16]$$

$$\eta_h = \tan^{-1}\left(\frac{V_x}{V_z}\right) \quad [17]$$

where v_x, v_y, and v_z are the velocity components of each ray in the x, y and z planes respectively. For this experiment a PSD and a divergence monitor were placed just before the sample. The monitors' width and height was set to be slightly larger than the height of the sample, at 45 x 45 mm to avoid detecting low-energy neutrons of high divergence that are not likely to hit the sample.

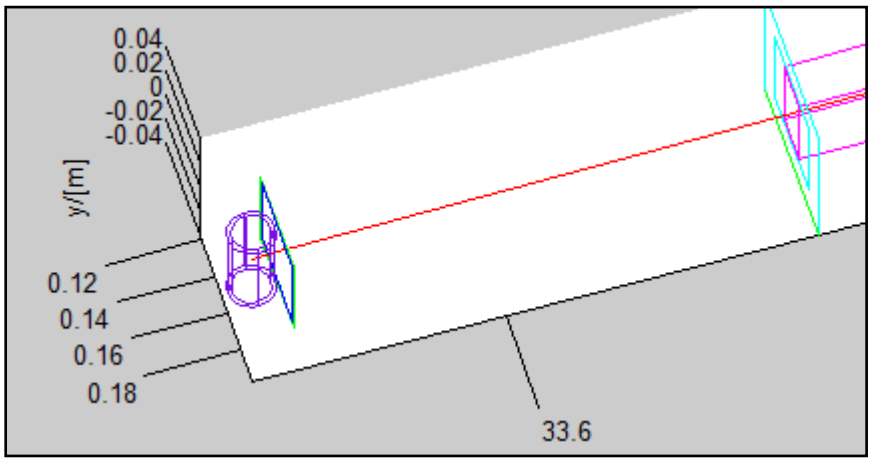

Figure 17: A schematic of the setup showing PSD and divergence monitors as rectangles just before the sample on the left and the tapered guide exit with more monitors on the right.

Simulated neutron count: 100 million.

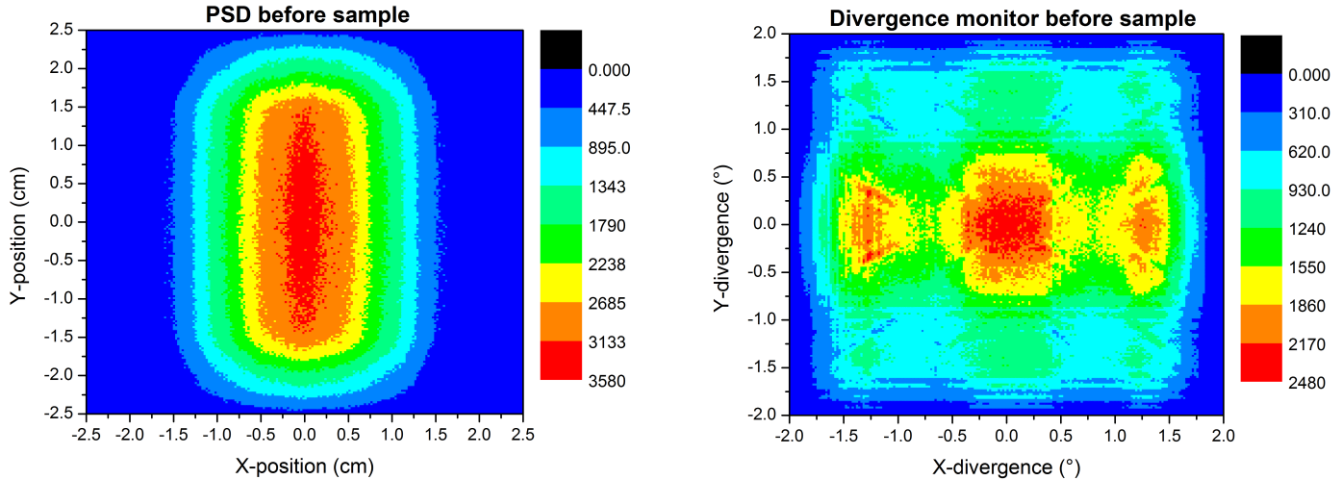

Figure 18: A PSD monitor on the left showing neutron intensity distribution as seen by the sample. The divergence monitor on the right shows that the majority of the neutron flux incident on the sample is of low divergence. Divergence along the x-axis shows a slight asymmetry. Again, this is expected because of the curvature of the guide along the x-z plane.

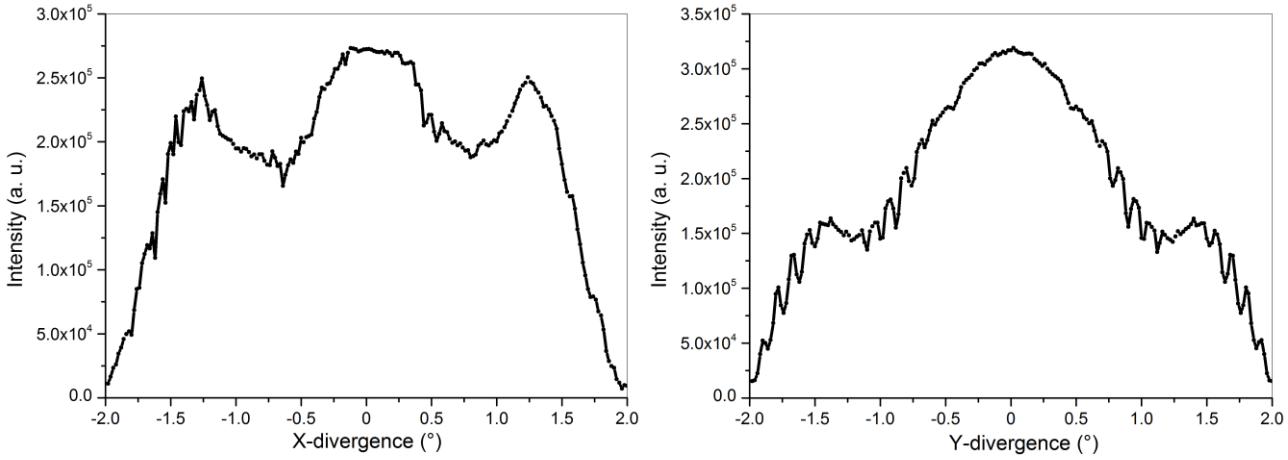

Figure 19: Total intensity as a function of the x & y divergence. These plots show a more quantitative approach in comparing divergence along the x and y divergence positions separately. Again a slight asymmetry in divergence along the x-axis is observed.

4.4.Sample

The sample can be a solid or a hollow cylindrical block of vanadium located 34 m away from the outer boundary of the moderator. It has an 11 mm outer radius and is 44 mm high. Vanadium is used due to its property of isotropic incoherent scattering. For the purpose of this model a hollow vanadium sample was used with an inner radius of 9mm (2mm thick), making it comparable to the vanadium sample used at OSIRIS. However, while on OSIRIS a hollow sample is used to minimize multiple scattering, the McStas vanadium component "V_sample" does not calculate multiple scattering, so using any thickness of the sample does not affect the results significantly.

4.5.Final spectroscopy detector

The spectroscopy detector had to be modelled before any analyser tests could be conducted. The detector is 39.12 mm high and 12.70 mm wide. Its exact position and rotation was unknown and had to be traced with the use of engineering specifications. It was traced to be located approximately 24.25 cm away from the sample along the x-axis towards the analyser crystals, and 11.50 cm below the sample along the y-axis. The rotation of the detector was set at approximately 4° clockwise.

4.6.Analyser array

An analyser crystal (known as monochromator in McStas) is the most important part in determining the instrument's energy resolution. Neutron scattering instruments are usually fitted with large arrays of analyser crystals for maximising experimental data. These crystals, depending on their position present data over a wide range of Bragg conditions relative to the sample tested. The analyser array present on OSIRIS occupies 40 rows by 226 columns and consists of PG crystals, each measuring 10 mm by 10 mm in height and width and 2 mm in thickness, covering scattering angles from 11° to 155°. Neutrons incident on

the analyser are near backscattered and energy analysed. The horizontal and vertical mosaic spread of the crystals is 0.8°. This assembly of crystals is mounted on an elliptically machined aluminium backing plate (8). In terms of focusing, the spectroscopy detectors pick up signals from all 40 rows vertically, but only from roughly 5 columns horizontally due to a radial collimator present on OSIRIS. In this sense, for the simulation purposes it is sufficient to use a single detector with an analyser array of 40 rows by 5 columns.

4.6.1. Comparing monochromator components

Firstly, the flat "Monochromator_flat", the curved "Monochromator_curved" and the polarising "Monochromator_pol" components were compared in terms of performance to decide which one is more suitable for modelling the PG assembly. The purpose of this short test was to run three separate simulations of the OSIRIS model but with only one analyser tile (perpendicular to the beam line) instead of the full 40 x 5 array. The polarising monochromator component was set to ignore polarisation effects. The monochromator d-spacing was set to 3.344Å.

Setup: O-SI-2526-364-05-F (averaged)
Simulated neutron count 3 billion

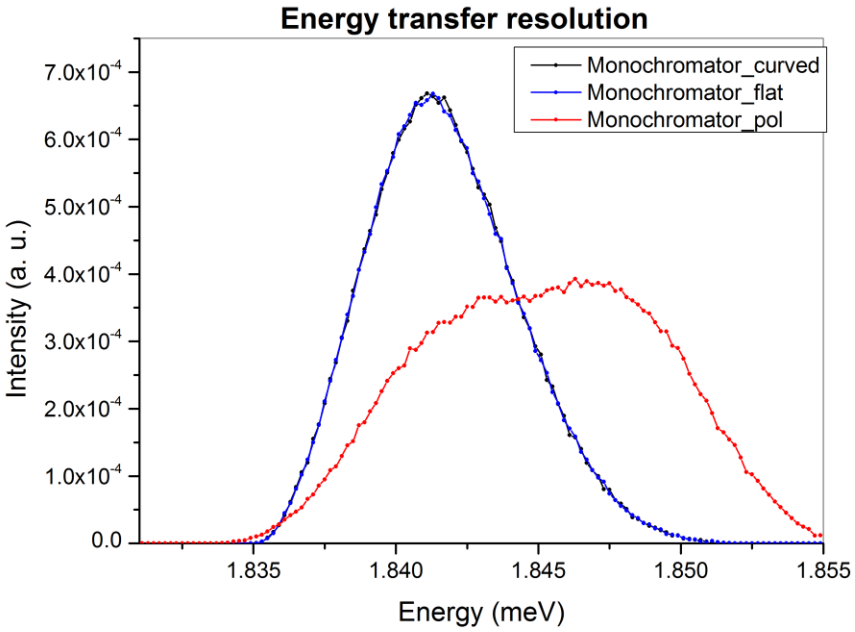

Figure 20: Energy transfer curves of the three monochromator components compared. The curved and flat monochromators show identical energy transfer curves, while the polarising component outputs different results.

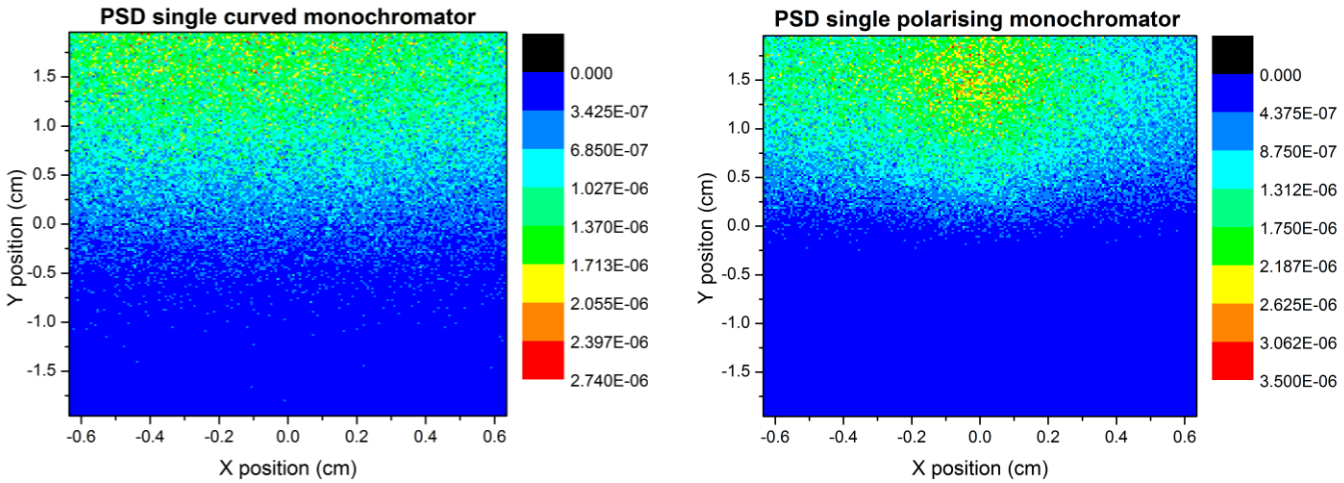

Figure 21: PSD distributions: left – curved monochromator, right – polarising.

The difference in performance between the curved and flat monochromator components proved to be minimal, within the statistical error. On the other hand the polarising monochromator showed very different energy resolution parameters. More will follow later in the report on the problematic behaviour of the polarising monochromator component. For convenience the curved monochromator was preferred over the flat due to the fact that the radius of curvature of graphite crystals at OSIRIS is constant horizontally, along each row. This means that each row containing 5 analyser crystals may be combined into one curved monochromator component made of 5 tiles. This reduces coding complexity and the total number of analyser tiles to be used from 200 to 40 and as will be seen later on, proved to increase computational efficiency approximately by a factor of two.

4.6.2. Analyser focusing tests

The purpose of this test was to observe the focusing saturation point of the spectroscopy detector as a function of number of analyser crystals modelled vertically and horizontally in an array. As each monochromator tile is rotated in such a way to focus a little further behind the detector, neutron count of the spectroscopy detector should fall dramatically after a certain threshold of tiles added horizontally. The test was performed using the Monochromator_curved and Monochromator_pol components. The horizontal and vertical angular tilts of the crystals were kept to the OSIRIS specification.

The interest for the polarising component lies in the fact that it is the only monochromator in McStas able to model crystal d-spread, which would allow for more accurate energy resolution modelling of OSIRIS. However, as was observed from these tests, the polarising monochromator showed unpredictable behaviour when modelled in an array of crystals of more than one tile.

Setup: O-SI-2526-364-05-F (averaged)

Simulated neutron count: 400 million

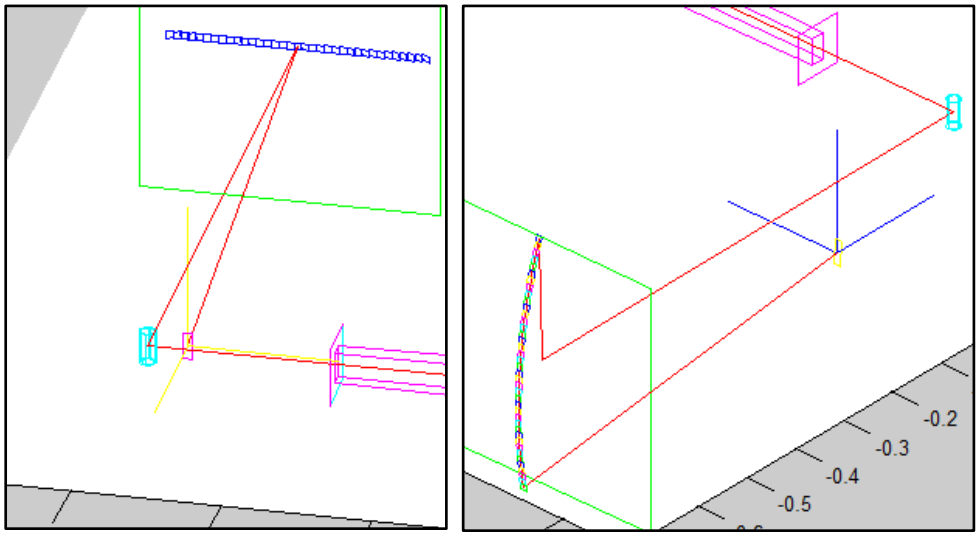

Figure 22: A schematic of the horizontal monochromator setup (left) with tiles spreading outwards from the central piece and of the vertical monochromator setup (right) with tiles spreading outwards vertically from the central piece.

4.6.2.1. Monochromator_curved

Horizontal setup

Note that when Monochromator_curved curves each generated tile along the axis by a specified angle it does not adjust the radii of each tile to correct for increase in distance from the sample. This setup is a little inaccurate as it's not spherical, but since the distance to the sample is many time greater than the width of the generated crystal array this inaccuracy becomes negligible.

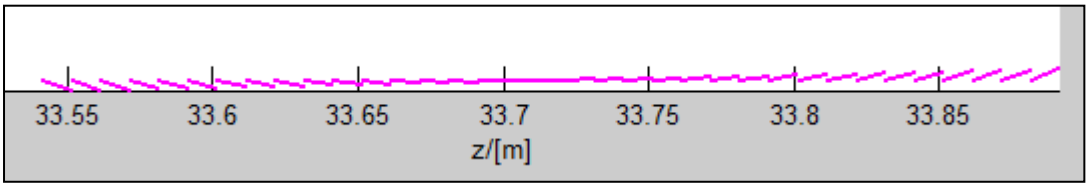

Figure 23: Illustration of the component's non-spherical curvature.

Number of tiles	Integrated intensity	Neutron count	Intensity increase ratio
1	0.0215185	2 639	1.00
2	0.043023	5 168	2.00
3	0.0657997	7 846	3.06
4	0.0847894	10 222	3.94
5	0.103744	12 650	4.82
6	0.125278	15 023	5.82
7	0.145873	17 390	6.78
8	0.160859	19 430	7.48
9	0.173831	21 122	8.08
10	0.18572	22 703	8.63
11	0.205784	24 495	9.56
12	0.218184	26 094	10.14
13	0.22293	26 992	10.36
14	0.237444	28 960	11.03
15	0.245323	29 989	11.40
16	0.256753	31 114	11.93
17	0.256928	31 607	11.94
18	0.279211	33 833	12.98
19	0.285957	34 731	13.29
20	0.291193	35 823	13.53
25	0.298923	36 167	13.89
30	0.295507	36 006	13.73
35	0.29796	36 099	13.85

Table 2: Results showing an increase in integrated neutron intensity as seen by the spectroscopy detector as a function of number of tiles placed outwards horizontally.

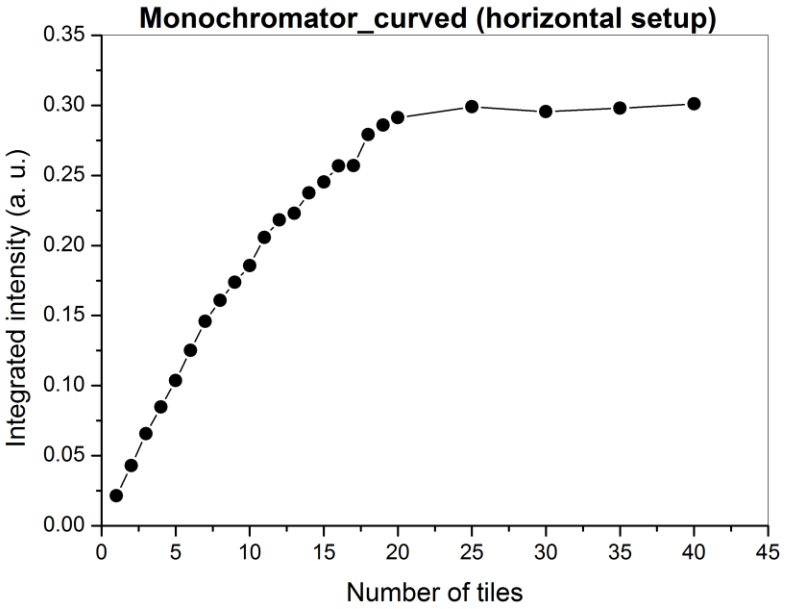

Figure 24: A plot showing the integrated neutron intensity as a function of number of tiles placed horizontally. It may be observed that the number of neutrons incident on the detector doesn't increase linearly with the number of tiles arranged horizontally.

Vertical setup

Number of tiles	Integrated intensity	Neutron count	Intensity increase ratio
1	0.0222688	2 443	1.00
2	0.0560529	6 149	2.52
3	0.0962899	10 623	4.32
5	0.172215	18 793	7.73
8	0.251384	27 591	11.29
10	0.324058	35 362	14.55
15	0.490846	53 709	22.04
20	0.643198	70 524	28.88
25	0.783223	86 479	35.17
30	0.940714	104 050	42.24
35	1.10217	122 385	49.49
40	1.19754	134 814	53.78

Table 3: Results showing the increase in integrated neutron intensity as a function of number of tiles placed outwards vertically.

For the vertical setup the increase in integrated neutron intensity almost follows a linear relationship. In fact, integrated intensity increases even by a bigger factor, compared to the increase in the number of tiles placed. This might be related with the geometry of the crystal array and how much signal the detector is able to pick up at various angles. The gain in signal from adding tiles at the bottom of the array outweighs the gain in signal from adding crystals at the top at an increasing rate with each tile placed at the bottom.

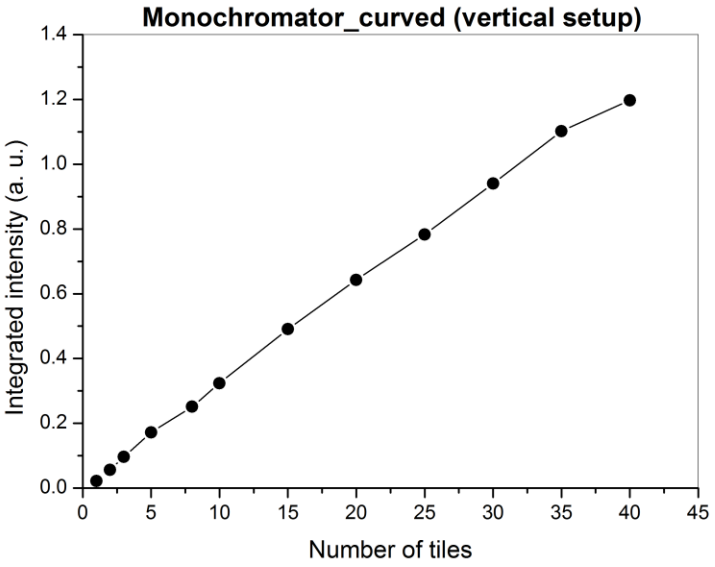

Figure 25: A plot showing integrated neutron intensity seen by the detector as a function of number of tiles placed vertically.

4.6.2.2. Monochromator_pol

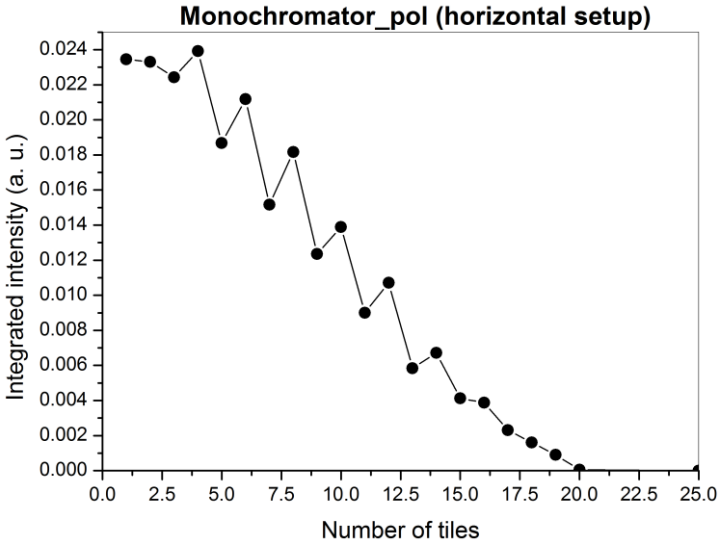

Figure 26: A plot showing integrated neutron intensity seen by the detector as a function of number of polarising tiles placed horizontally. The puzzling effect observed is the decrease in intensity with more tiles added. In fact intensity should increase in a similar manner to the curved component.

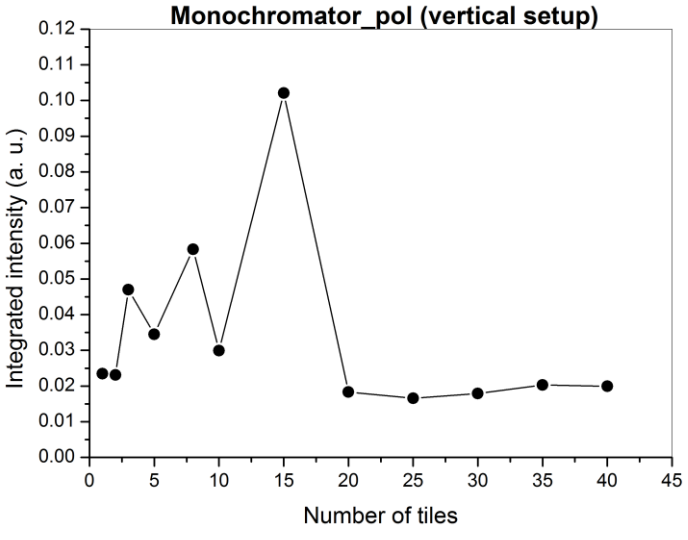

Figure 27: A plot showing integrated intensity of neutron flux seen by the detector as a function of number of polarising tiles placed vertically. Again results are non-intuitive. This time results look even more unpredictable.

4.6.3. Analyser mosaic spread tests

Crystal mosaic spread is defined as angular deviation of crystal lattice plains from a perfectly ordered crystal structure. The PG analyser crystals used in OSIRIS have a mosaic spread of 0.8° both along their horizontal and vertical planes. Different mosaic orientations hence reflect beams of varying divergence into the spectroscopy detector at different Bragg angles. The aim of this test is to find the most effective mosaic spread at which neutron intensity reaches a maximum for OSIRIS as mosaic spread is one of the quantities that may be adjusted in order to better match OSIRIS's resolution function. The input moderator energy range was left at 1.5 – 2.5 meV as this distribution was wide enough to account for the change in θ due to mosaic ranges presented in the test.

Setup: O-SI-2526-364-05-F (averaged)
Simulated neutron count: 200 million
Monochromator offset angle: 3.991°

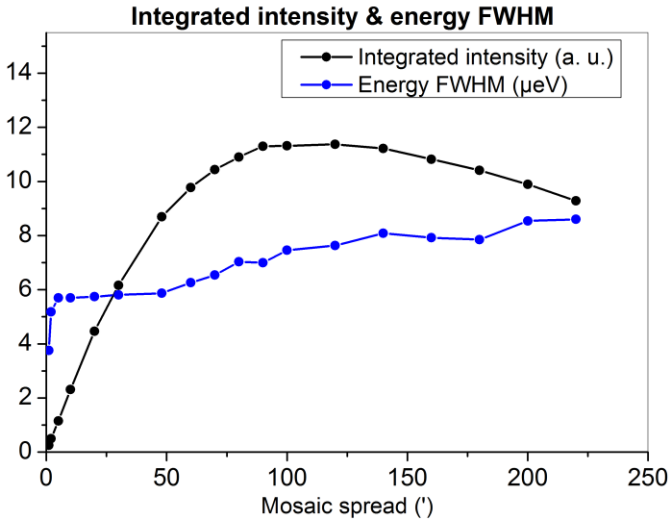

Figure 28: A plot showing intensity and energy FWHM values for the range of crystal mosaic values. Two important conclusions result: the energy resolution curve broadens slightly with increase in mosaic spread and the neutron flux is maximised for the mosaic range of approximately 90' to 120'.

It may be observed that energy FWHM increases slightly with an increase in crystal mosaic spread. This is expected due to the fact that higher mosaic ranges broaden the energy distribution of the Bragg reflected neutrons. There is however a limitation in the range of Bragg angles picked up by the detector. It may be noted that according to the simulation the most efficient setup is at the mosaic spread values of approximately 90' to 120' where the neutron flux is maximised. However, this of course does not take into account the manufacturing availability of PG of these properties.

4.6.4. Modelling the analyser crystal assembly

The crystal assembly was modelled by 40 rows with 5 columns. The array was modelled initially using one flat monochromator component per tile, adding 200 components to the instrument definition.

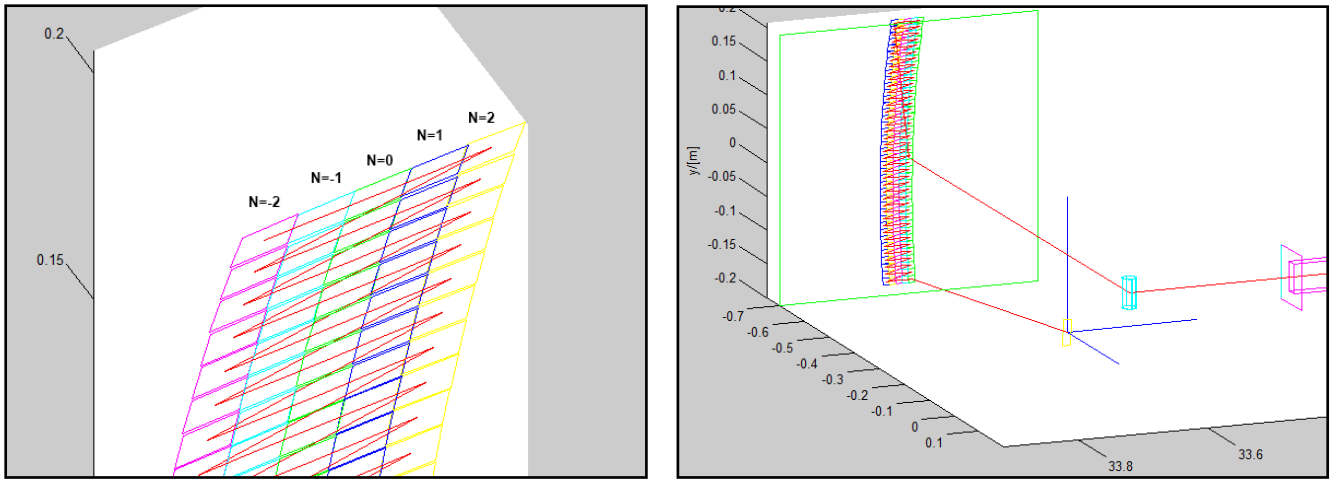

Figure 29: On the left an illustration of how angular rotation was applied horizontally. The horizontal radius of curvature was assumed to be around 0.866m for all 40 rows. This produced a factor of N × 0.66° increase in angular rotation for each tile placed horizontally. Each tile was treated as a separate component and had to be rotated by a certain angle. On the right a schematic of the OSIRIS secondary spectrometer with all 200 tiles, with the cylindrical sample in the centre, guide exit on the right and the spectroscopy detector below the sample.

Note that the O-SI-2526-364-05-F (averaged) engineering specification referred to throughout this report does not actually contain the word “averaged” in its title, but it was added to make a clear distinction between the two engineering setups used throughout this report, which otherwise only differ slightly in their names. The O-SI-2526-364-05-F (averaged) engineering specification was discovered before the SI-2526-364-03-E specification and appears to present smoother analyser crystal angles than the latter, hence the inclusion of the word “averaged” in its title.

4.6.5. Alternative analyser assembly setup with “Monochromator_curved” component

Later the setup was simplified by unifying all the horizontal monochromator tiles into one component per row instead of five, thanks to the curved monochromator component instead of the flat one. This was also possible because horizontal angular deviation was constant for each row, unlike the vertical angular deviation. Vertical angles and distances to the sample were modelled this time using the *SI-2526-364-03-E* engineering specification.

Horizontal angular parameters have to be specified in the form of a radius of curvature for the curved monochromator. This was found in the *SI-2526-364-05-F (averaged)* engineering specification. According to it the radius of curvature of the topmost crystal is 0.86596 m, while for the bottommost it is 0.90927 m. These two values were taken and divided into three steps, with one value in-between the two, and distributed equally amongst the 40 rows. The first 13 rows were assigned the 0.866m radius of curvature, the bottom 13 rows - 0.909 m, and the middle 14 rows – 0.888 m. In all those calculations the sample was the point of focus, from where the radii of curvature were assumed. See *appendix 1* for more technical information on the crystal parameters.

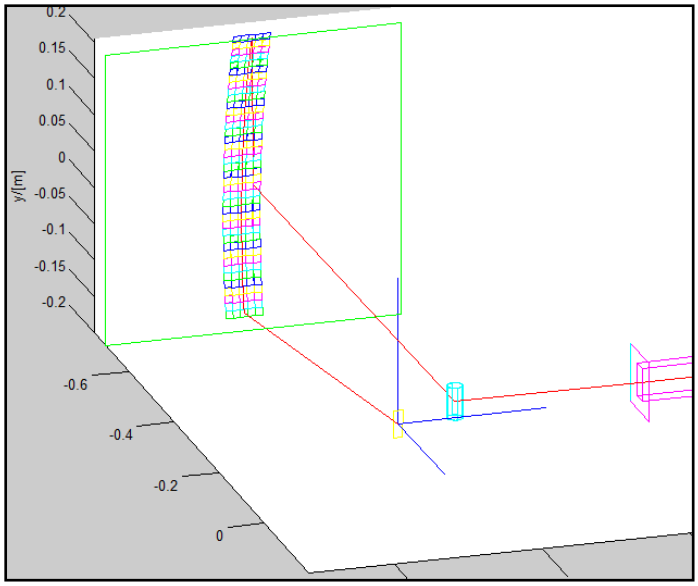

Figure 30: A schematic of the OSIRIS secondary spectrometer simplified to 40 tiles using the curved monochromator component. Each row now contains one component instead of five.

4.6.6. Comparing the 200 tile with the 40 tile analyser setup

Simulated neutron count: 500 million

	Time taken (s)	Integrated intensity	Neutron count	Intensity increase ratio
200 tiles (Monochromaor_flat)	3 570	5.85232	5 824	1
40 tiles (Monochromator_curved)	1 716	5.80096	5 873	2.06

Table 4: Results showing a twofold increase in computational efficiency for the 40 tile setup.

4.6.7. The SI-2526-364-03-E specification

The SI-2526-364-03-E engineering specification was the first specification based on which the full analyser crystal array was modelled. The first complete OSIRIS setup was then simulated to observe its resolution. Results are presented in the figures below.

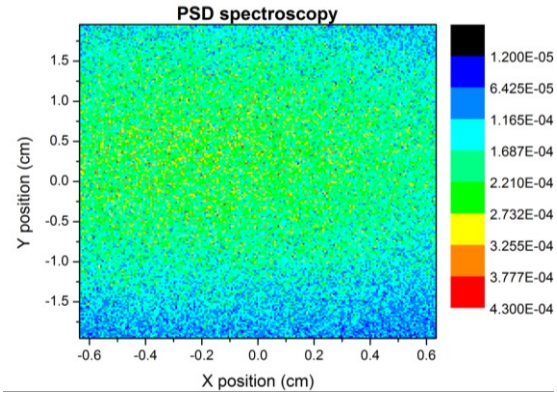

Figure 31: A PSD monitor showing neutron intensity distribution as detected by the spectroscopy detector. This setup focuses well, although the focus point is slightly shifted top-left from the centre of the detector.

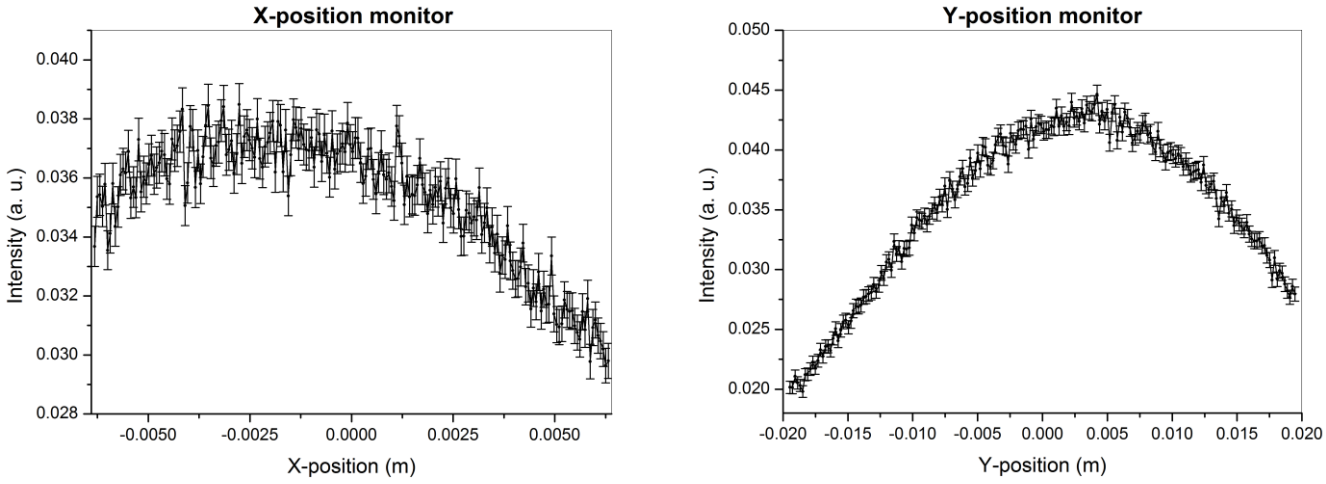

Figure 32: Intensity distribution along the x and y positions of the spectroscopy detector. Asymmetry of the lineshapes is an indication that the neutron flux is not focused exactly at the central point of the detector and is a tool for quantitatively evaluating the performance of the setup.

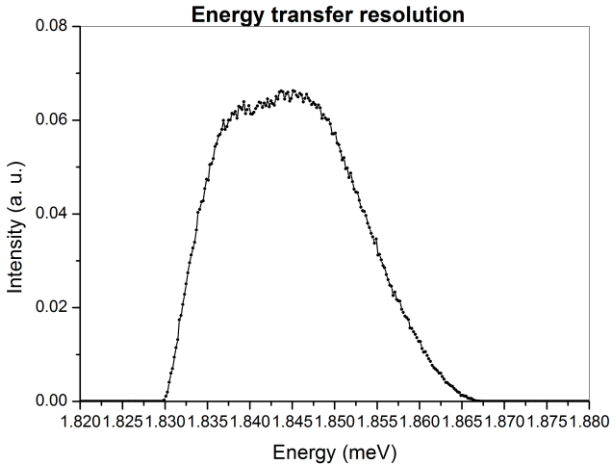

Figure 33: An energy resolution plot of the spectroscopy detector with energy FWHM of 21.5μeV. "E_monitor" was used; it presents results directly in energy without converting from time-of-flight.

4.6.8. The SI-2526-364-05-F (averaged) specification

The SI-2526-364-05-F (averaged) engineering specification, as mentioned earlier, features a "smoother" transition in vertical angular tilt of the crystals, while in the other specification many of the crystals have duplicate angular tilt values. Hence this specification may be an approximation of the real case. Results of both specifications are compared below.

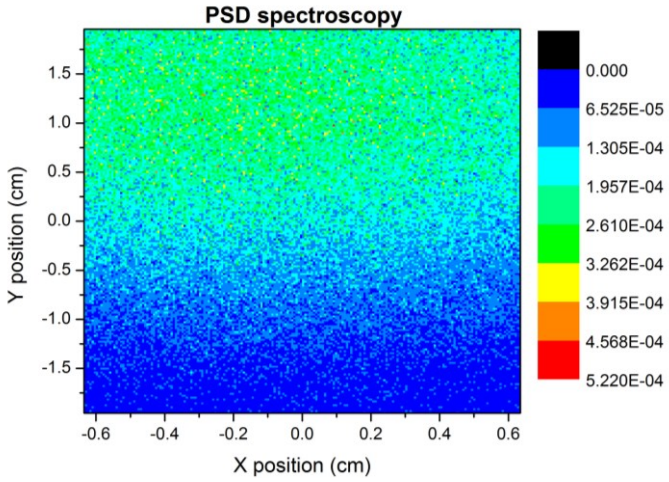

Figure 34: A PSD monitor showing neutron intensity distribution as seen by the spectroscopy detector. This setup is significantly more out of focus than the SI-2526-364-03-E setup.

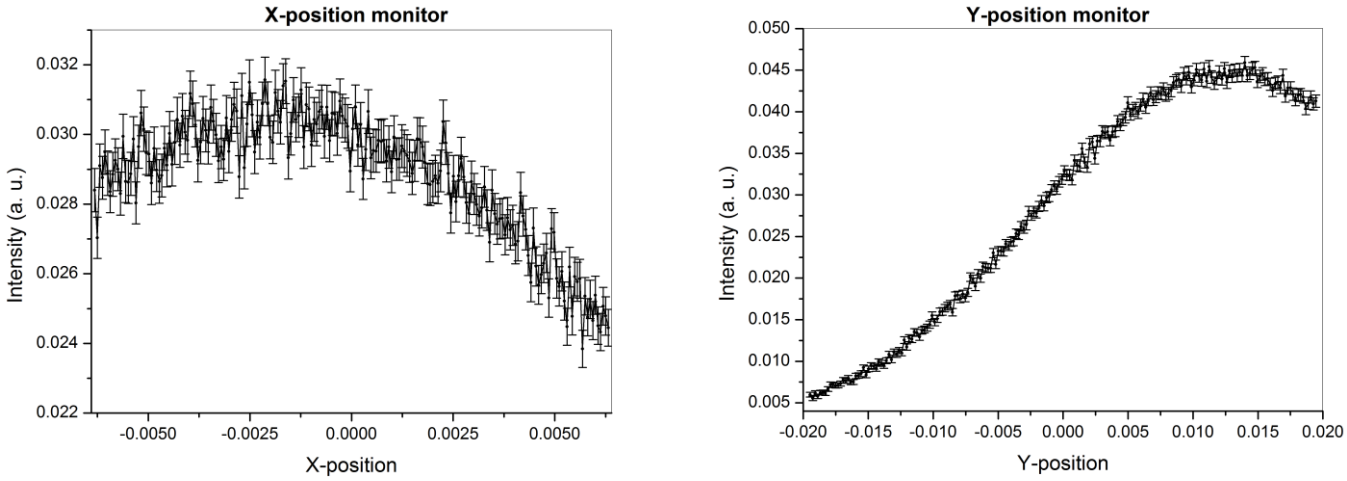

Figure 35: Intensity distribution along the x and y position of the spectroscopy detector. This setup focuses much worse along the y-axis, suggesting that the vertical crystal tilt is not well optimised.

The averaged angle specification proved to focus the beam poorly along the vertical y-axis, so in the end it did not come out as an improvement to the *SI*-2526-*364-03-E* specification presented earlier. The energy monitor measured energy FWHM to be 20.80 µeV for the *SI-2526-364-05-F (averaged)* setup, compared to 21.52 µeV for the previous *SI*-2526-*364-03-E* setup. This latter proved to give a larger energy FWHM value as well as more neutron flux focused on the detector.

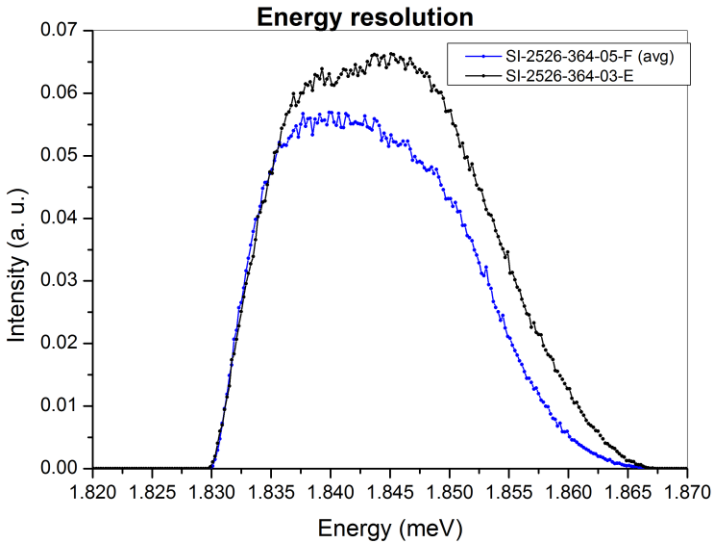

Figure 36: An energy resolution plot of the energy monitor for both setups with energy FWHM values of 21.5 μeV for the SI-2526-364-03-E setup and 20.8 μeV for the SI-2526-364-05-F (averaged) setup. That's a approximately 3% decrease over the previous setup.

4.6.9. Realigning analyser crystals to increase FWHM of ΔE

Since the *SI-2526-364-05-F (averaged)* specification does not focus well onto the spectroscopy detector along the vertical y-axis, the vertical angular tilt values of crystals were tweaked manually to observe how this can affects the FWHM values of energy at various angles. The angular tilt was changed by a constant value going in steps of 10 rows at a time. Negative angular deviation means the tiles were focused more downwards from the sample (which helped the top 20 crystals to produce better focus), while positive – upwards (which helped the bottom 20 crystals).

Tiles 1-10			
Angular offset (°)	**Integrated intensity**	**Neutron count**	**Energy FWHM (μeV)**
-0.6	6.72755	415 603	23.4
-0.7	6.72844	417 015	23.7
-0.8	6.79186	419 438	23.7
-0.9	6.76402	417 638	24.1
-1.0	6.6527	411 191	24.3
-1.1	6.57256	405 037	24.7

Tiles 11-20			
Angular offset (°)	**Integrated intensity**	**Neutron count**	**Energy FWHM (μeV)**
-0.5	6.48824	398 856	21.5
-0.6	6.51456	401 370	21.8
-0.7	6.56521	403 147	21.2
-0.8	6.54706	401 569	21.8
-0.9	6.49225	399 525	22.2
-1.0	6.4022	394 431	21.6

Tiles 21-30			
Angular offset (°)	**Integrated intensity**	**Neutron count**	**Energy FWHM (μeV)**
0.6	5.08955	314 594	22.2
0.7	4.98458	308 718	22.4
0.8	4.90482	303 362	22.2
0.9	4.7995	297 454	22.2
1.0	4.71505	292 292	22.0
1.1	4.63269	288 135	22.5

Tiles 31-40			
Angular offset (°)	**Integrated intensity**	**Neutron count**	**Energy FWHM (μeV)**
0	5.75762	356 129	20.6
0.1	5.69181	351 361	20.6
0.2	5.59943	346 031	21.0
0.3	5.52096	339 750	20.8
0.4	5.41689	336 047	20.4
0.5	5.34504	329 605	20.0

Table 5: Energy FWHM values as a result of in introducing an offset in crystal tilt.

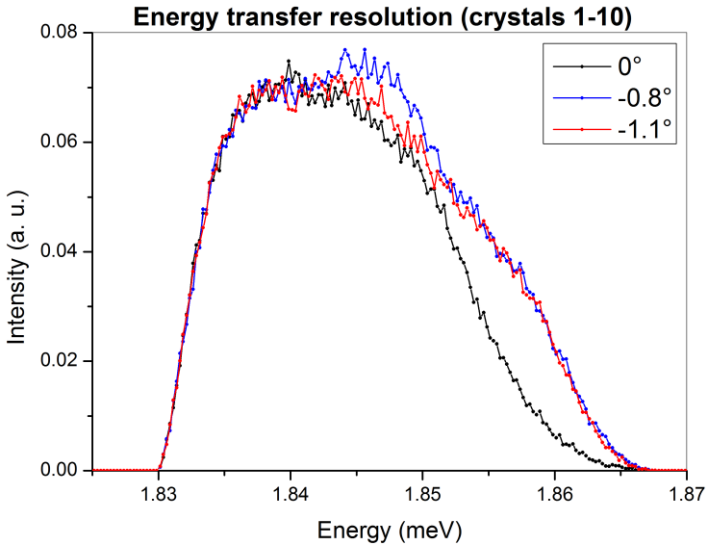

Figure 37: Introducing a tilt offset on the top 10 crystals made more difference to the energy resolution curve than for any other crystals. This means that top crystals in the SI-2526-364-05-F (averaged) specification are not focused well enough on the detector. By tilting the crystals downwards from 0° up to -1.1°, energy FWHM values of 20.8μeV to 24.7μeV are obtained respectively, accounting for approximately a 19% increase in FWHM.

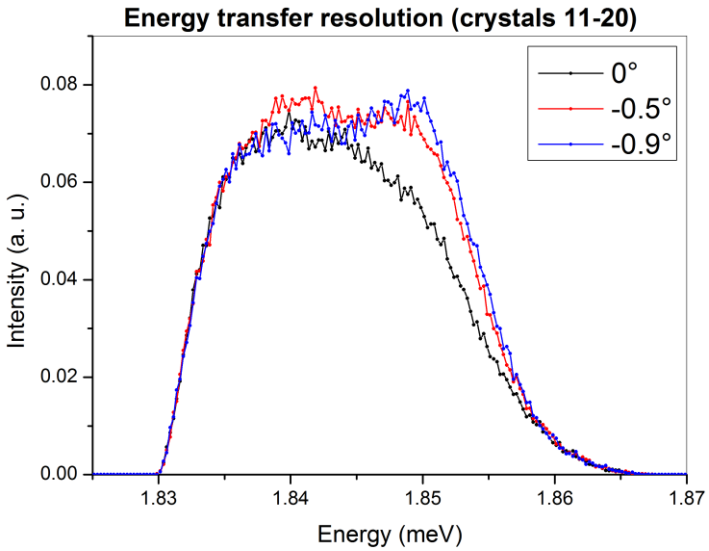

Figure 38: The second set of 10 crystals did not produce as much increase in energy FWHM, ranging from 20.80μeV for no tilt to 22.20μeV for the -0.9° tilt, which accounts for an approximately 7% increase in FWHM.

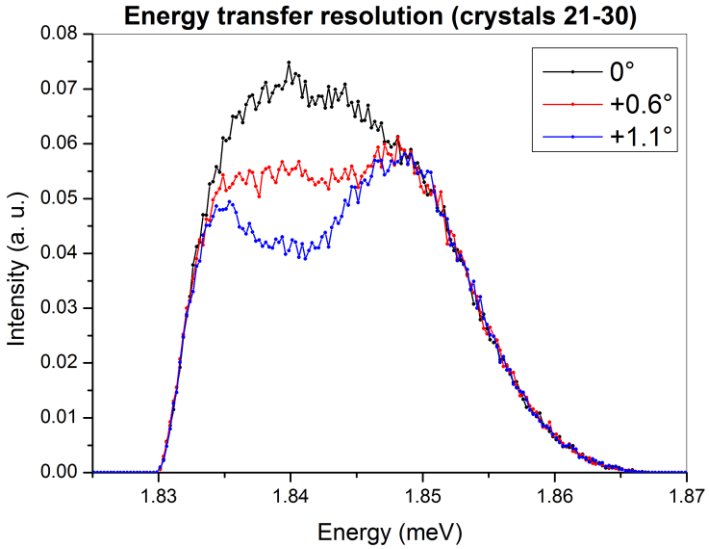

Figure 39: Little change in energy FWHM is observed: 20.80μeV for no tilt to 22.47μeV for the +1.1° tilt, which accounts for an approximately 8% increase in FWHM.

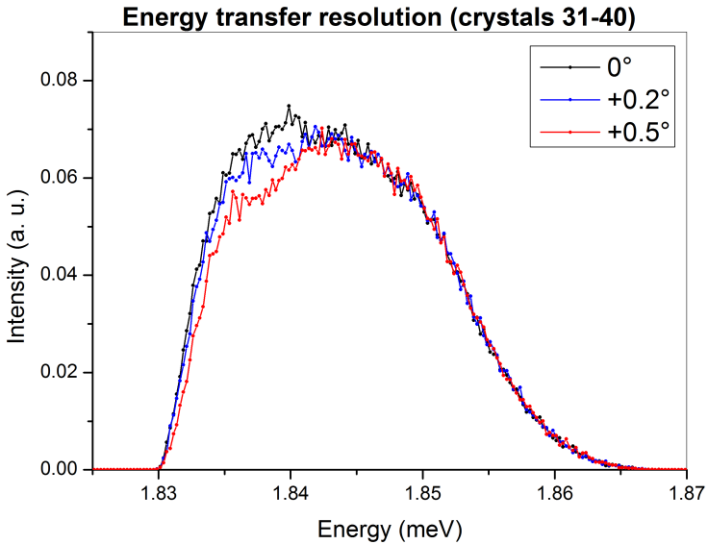

Figure 40: The least change in energy FWHM out of all setups: from 20.80μeV for no tilt to 21.01μeV for the +0.2° tilt, which accounts for a 1% increase in energy FWHM. Hence the bottom set of 10 crystals focus well at its original tilt values.

4.6.10. Better focusing with the 4.65° offset setup

According to the *RAL-TR-2004-021* report on OSIRIS, the vertical offset of the perpendicular to the sample crystal is specified to be around 4.65°. This value was assumed to correspond to the Bragg angle of 85.35°. However, the *O-SI-2526-364-05-F (averaged)* engineering specification lists the angle of one of the central tiles to be 3.991°, so the tilt difference of approximately 0.66° between the two values was added to tilt values of all crystals above the 3.991° crystal, inclusive, and subtracted for all the crystals below the 3.991 crystal.

The new setup focuses better than the *SI-2526-364-05-F (averaged)* setup. Still, the x and y position distributions do not look as symmetrical as they could be. The signal is out of focus mostly along the y-axis as can be seen on Figure 42: x & y position monitors. Signal distribution looks very similar to the SI-2526-364-03-E setup. Focusing of the crystals is improved from the SI-2526-364-05-F (averaged) setup in.. The new setup also increases neutron intensity by around 30% over the previous one. This setup resembles closely the original SI-2526-364-03-E setup in terms of focusing.

Setup	TOF FWHM (μs)	Energy FWHM (μeV)	Integrated intensity	Neutron count
SI-2526-364-03-E	343.0	21.5	7.08914	2 186 820
SI-2526-364-05-F (averaged)	330.1	20.8	5.77244	1 779 520
4.65° offset	344.0	22.1	5.60838	2 396 140

Table 6: TOF & energy FWHM values for each of the three analyser crystal setups.

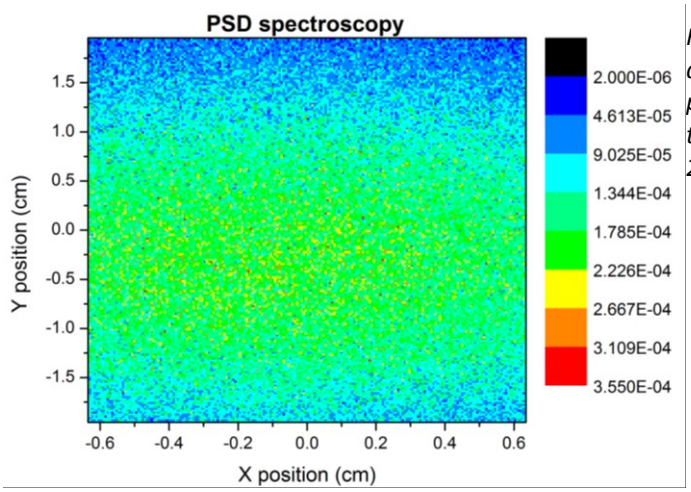

Figure 41: PSD distribution of the spectroscopy detector, looks more in focus compared to the previous SI-2526-364-05-F (averaged) setup. In terms of focusing it resembles closely the SI-2526-364-03-E setup.

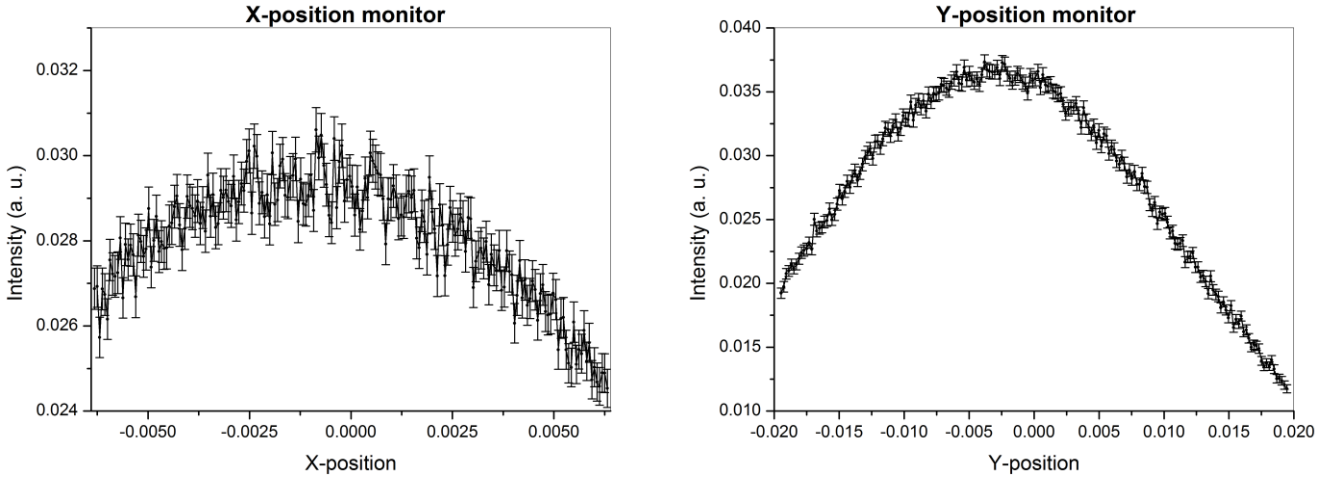

Figure 42: x & y position monitors. Signal distribution looks very similar to the SI-2526-364-03-E setup. Focusing of the crystals is improved from the SI-2526-364-05-F (averaged) setup in.

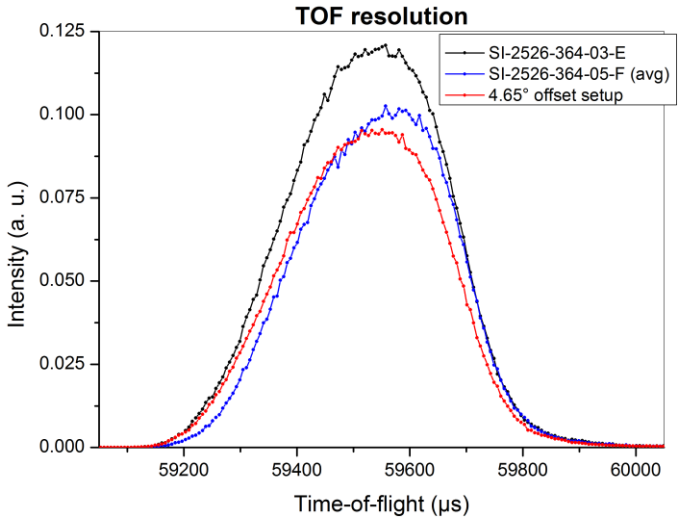

Figure 43: Time-of-flight resolution curves of the three setups. TOF FWHM values are 343.0 μs [SI-2526-364-03-E], 330.1 μs [SI-2526-364-05-F (averaged)] and 344.0 μs [4.65° offset setup]. This constitutes a maximum difference of approximately 4% between the three.

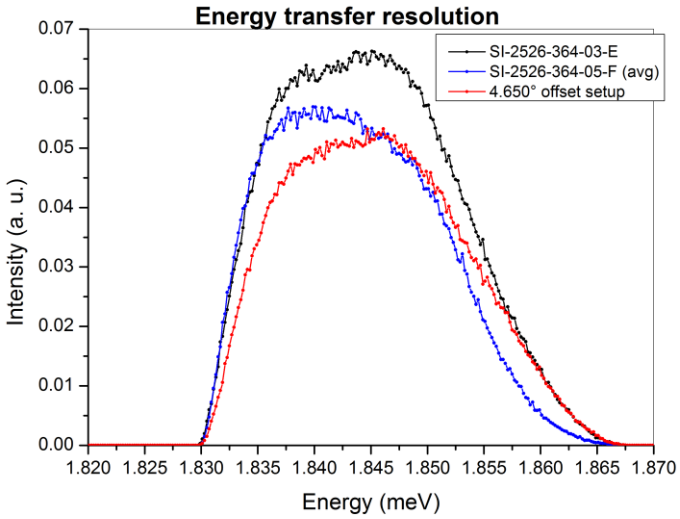

Figure 44: Energy resolution curves for the three setups. The energy FWHM values are 21.52 μeV [SI-2526-364-03-E], 20.80μeV [SI-2526-364-05-F (averaged)] and 22.06 μeV [4.65° offset]. This constitutes a maximum difference of approximately 6% between the three.

4.6.11. Multiple monochromator setup

4.6.11.1. Testing the setup

One other contributing factor to the resolution curve which has not been discussed in detail yet is the crystal d-spread. Unfortunately none of the curved of flat monochromator components in McStas have an option to specify a d-spread. One trick to overcome this limitation without modifying the code of the components was to place two more monochromator tiles behind the existing one, making a layer of three tiles for each row, and setting a different value of d-spacing for each. The interesting thing is that McStas allows propagation of neutrons through multiple tiles of monochromator crystals, even when the maximum reflectivity of each is set to one.

On the downside this method is very crude and lacks accuracy as the stepping size for d-spread is big. Adding more monochromator tiles is not a good solution as it is very time intensive to modify each tile separately in case something has to be changed, and because they increase complexity of the instrument by a lot, which leads to compilation errors due to McStas memory restrictions.

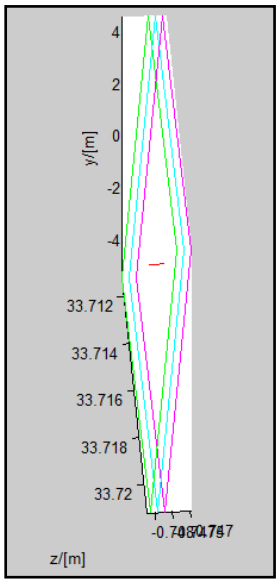

Figure 45: A schematic showing an example of the multiple tile setup of one crystal with two more added behind. Note that the distance between the tiles is exaggerated in the figure to make it clearer.

This setup first had to be evaluated to ensure there is no bias in the neutron intensity with each subsequent tile, and that the tiles work independently and do not influence each other in any way. A set of tests were performed with three tiles; the first tile having a d-spacing value of 3.344 Å, the second one - 3.844 Å, and the third one - 2.844 Å. This produced a large d-spread, enough to resolve three separate energy peaks. The McStas “SPLIT” command was also used from here onwards to enhance statistics and reduce simulation time.

Setup: SI-2526-364-03-E

Simulated neutron count: 200 million

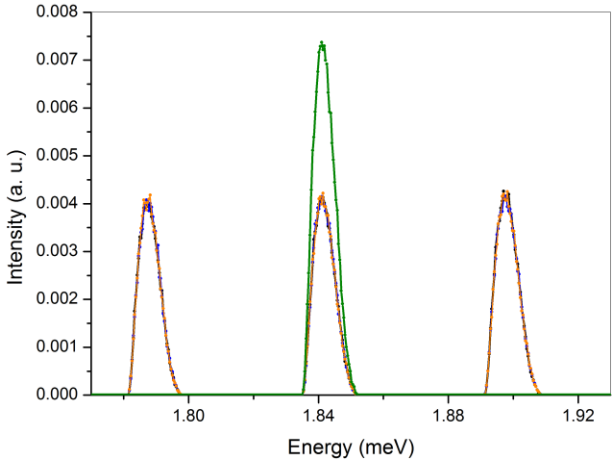

Figure 46: As may be observed from the graph three separate simulations with each tile's reflectivity set to 1 have produced identical energy peaks of same intensity. The green energy curve (corresponding to the central energy curve) is from a simulation with reflectivity of the last two tiles set to 0, but shows higher intensity with the other tiles disabled.

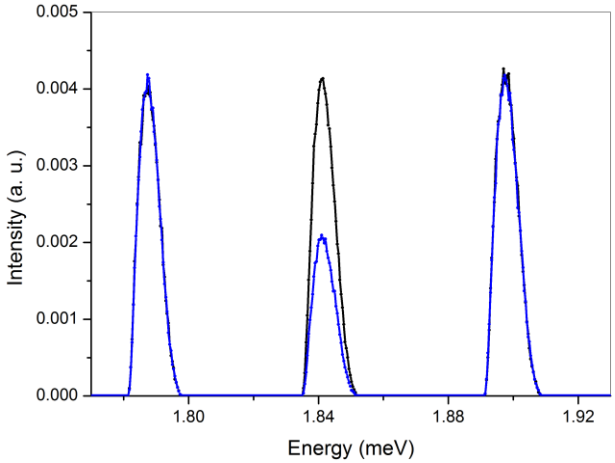

Figure 47: Another quick test was performed, this time setting the reflectivity of the first tile (corresponding to the central energy curve) to 0.5. In black: how it looks with reflectivity set to 1 for all three slabs, in blue – reflectivity with the first slab set to 0.5. Results are predictable.

4.6.11.2. Full simulations

Continuing from the previous investigation, a full set of simulations was carried out simulating OSIRIS with 3 analyser tiles in total per each crystal in the 40 x 5 analyser assembly. In general two observations follow from increasing d-spread. Firstly, neutron intensity increases, because the detector sees a broader incoming range of energies, although limited by its dimensions on the Bragg conditions it can pick up. Secondly, energy resolution increases in general for higher d-spread values, leading to an increase in energy FWHM values.

Setup: SI-2526-364-03-E

Simulated neutron count: 250 million

d-spread: Δd/d	Δd (Å)	±d (Å)	Integrated intensity	Neutron count	Energy FWHM (μeV)
0	0	0.000000	5.48227	693 476	21.65
1.0×10^{-3}	0.003344	0.001672	7.31997	1 133 440	21.75
1.25×10^{-3}	0.00418	0.002090	7.95637	1 231 790	21.39
2.5×10^{-3}	0.00836	0.004180	10.4129	1 609 400	21.40
3.0×10^{-3}	0.010032	0.005016	10.9573	1 694 330	21.77
4.0×10^{-3}	0.013376	0.006688	11.4912	1 778 090	23.31
5.0×10^{-3}	0.01672	0.008360	11.678	1 804 800	25.49
6.0×10^{-3}	0.020064	0.010032	11.741	1 813 980	27.80

Table 7: Results showing the effect of analyser d-spread on neutron intensity and energy FWHM values.

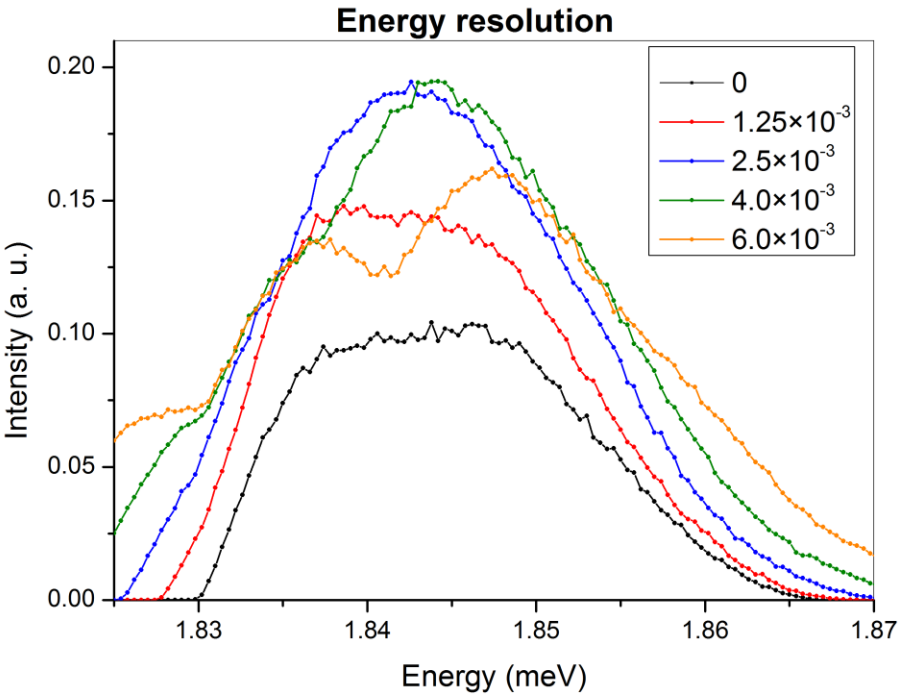

Figure 48: Energy resolution plot for each of the d-spreads. The shape of the energy curve changes considerably with an increase in d-spread.

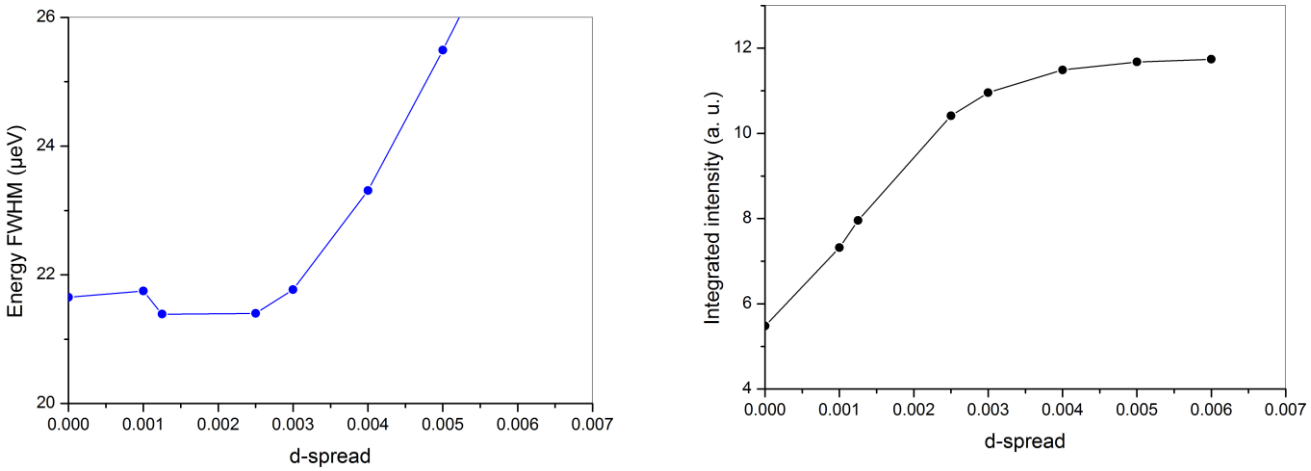

Figure 49: The energy FWHM and integrated intensity plots. Energy FWHM values fall slightly for a small increase in d-spread, and increase significantly for higher d-spread values. Integrated intensity increases as expected, with the rate of increase approaching zero at higher d-spread values.

4.6.12. Testing vanadium sample thickness

A few short tests were run to observe what effects changing vanadium sample thickness has on the energy resolution. Five different sample thicknesses were tested, ranging from 1mm to 11mm. In the simulations it was found that the thinner the sample, the more symmetric is the resulting neutron distribution incident on the analyser array. Also decreasing thickness leads to a slight decrease in neutron intensity as more of the incoming neutrons are able to penetrate the sample without reflecting. Note that from here onwards the final spectroscopy detector was moved from 12cm below the sample along the y-axis, as was the case in the previous experiments, to 11.7cm as it was thought that the latter value was more representative of the real case.

Setup: SI-2526-364-03-E

Simulated neutron count: 1.5 billion

Vanadium sample thickness (mm)	Energy FWHM (μeV)	Integrated intensity	Neutron count
1	22.44	5.30381	3 830 460
2	22.37	7.24345	3 913 170
4	22.28	8.15196	4 063 270
8	22.32	7.77123	4 235 720
11	22.22	7.61357	4 264 540

Table 8: Energy FWHM values as a function of vanadium sample thickness. Decreasing thickness leads to a subtle broadening of the energy curve. However the difference in FWHM values is so small that it may well be considered within statistical error. The main point here is that changing the sample thickness hardly affects OSIRIS's resolution.

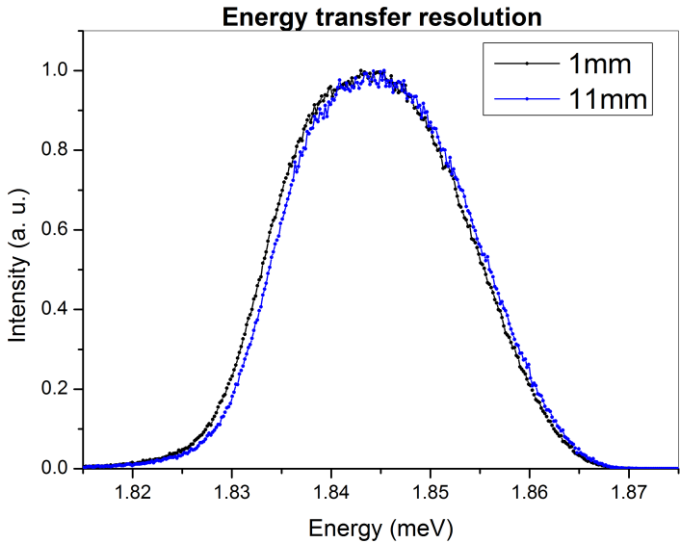

Figure 50: The energy FWHM values differ the most between the thinnest and the thickest samples: from 22.44 μeV for the 1 mm thick sample to 22.22 μeV for the 11 mm thick sample. However this only constitutes to about 1% difference in the FWHM values.

4.6.13. Sample height tests

A few more tests were carried out to see what effect changing the sample's length has on the energy FWHM values. For this purpose the sample was made shorter and longer than the standard size along the y-axis. Note that the tapered guide dimensions have not been altered, which is a limitation for long sample heights.

Setup: SI-2526-364-03-E

Sample height (mm)	Energy FWHM (μeV)	Integrated intensity	Neutron count
10	21.6	1.30995	2 483 390
34	22.3	3.78147	3 481 850
44	22.5	4.33963	4 024 270
54	23.1	4.12812	3 977 960

Table 9: Energy FWHM as a function of vanadium sample height.

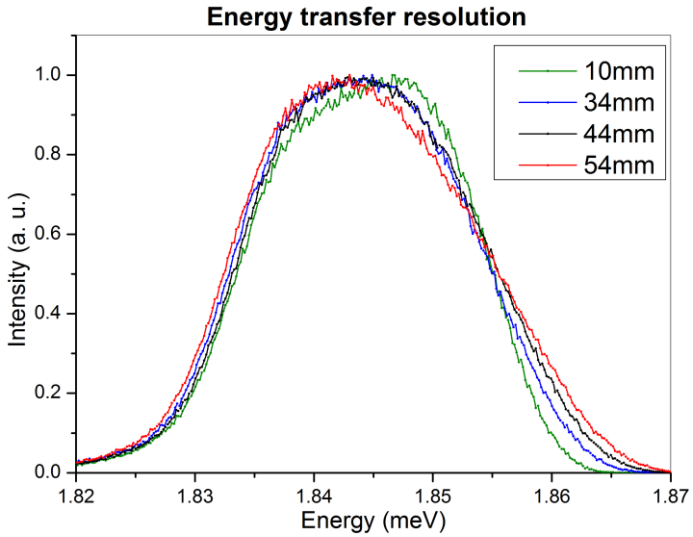

Figure 51: A graph showing the energy resolution curves for each of the sample highs. A definite increase in energy FWHM values can be observed as a result of prolonging the sample.

4.6.14. Calculating the Bragg condition of each analyser

This short investigation was carried out to observe how the reflected Bragg condition varies for each crystal throughout the assembly. Calculations were made to find the trigonometric angles that focus perfectly onto the spectroscopy detector, assuming the sample, crystal and detector geometries to be point-like. Therefore this is a rough approximation. As can be seen the maximum Bragg angle is 87.27° corresponding to the bottom crystal and decreases upwards to 83.05° for the top crystal. This gives the maximum Bragg difference of 4.22° for the crystal assembly.

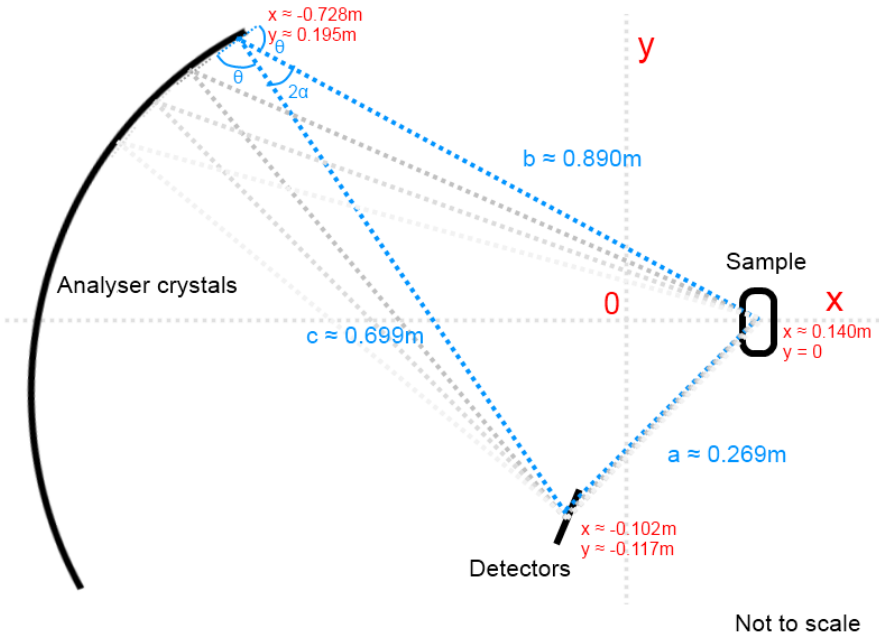

Figure 52: A sketch of the OSIRIS secondary spectrometer in the x-y plane illustrating how the Bragg angles were calculated. Sample, analyser and detector geometries were ignored. Bragg values were obtained trigonometrically by calculating lengths a, b, c, using the cosine rule to find the 2α angle and subtracting α from 90° to obtain the mean Bragg angle ϑ for each crystal.

Vertical tile position (cm)	Vertical angular deviation (°)	Mean Bragg angle (°)
19.5	18.811	83.05
18.5	18.811	83.14
17.5	18.397	83.24
16.5	16.666	83.33
15.5	16.666	83.42
14.5	15.925	83.52
13.5	14.518	83.62
12.5	14.518	83.71
11.5	13.512	83.81
10.5	12.384	83.91
9.5	12.384	84.01
8.5	11.125	84.11
7.5	10.256	84.21
6.5	10.256	84.32

Vertical tile position (cm)	Vertical angular deviation (°)	Mean Bragg angle (°)
5.5	8.829	84.32
4.5	8.12	84.42
3.5	8.12	84.52
2.5	6.53	84.63
1.5	5.985	84.74
0.5	5.985	84.84
-0.5	4.25	84.95
-1.5	3.855	85.06
-2.5	3.855	85.17
-3.5	1.982	85.28
-4.5	1.726	85.39
-5.5	1.726	85.50
-6.5	-0.278	85.61
-7.5	-0.4	85.73

Vertical tile position (cm)	Vertical angular deviation (°)	Mean Bragg angle (°)
-8.5	-0.4	85.95
-9.5	-2.53	86.07
-10.5	-2.53	86.19
-11.5	-2.703	86.30
-12.5	-4.66	86.42
-13.5	-4.66	86.54
-14.5	-5.005	86.66
-15.5	-6.791	86.78
-16.5	-6.791	86.90
-17.5	-7.333	87.02
-18.5	-8.928	87.14
-19.5	-8.928	87.27

Table 10: Data showing crystal positions and their corresponding vertical angular deviations according to the SI-2526-364-03-E specification, as well as the calculated Bragg angles for each of the crystals.

A simulation was ran testing only the 10 central tiles and comparing the energy FWHM values to a 1 tile as well as a full 40 tile simulation to get an estimate of how the number of tiles used vertically contribute to the instrument's resolution.

Setup: SI-2526-364-03-E

Simulated neutron count: 2 billion

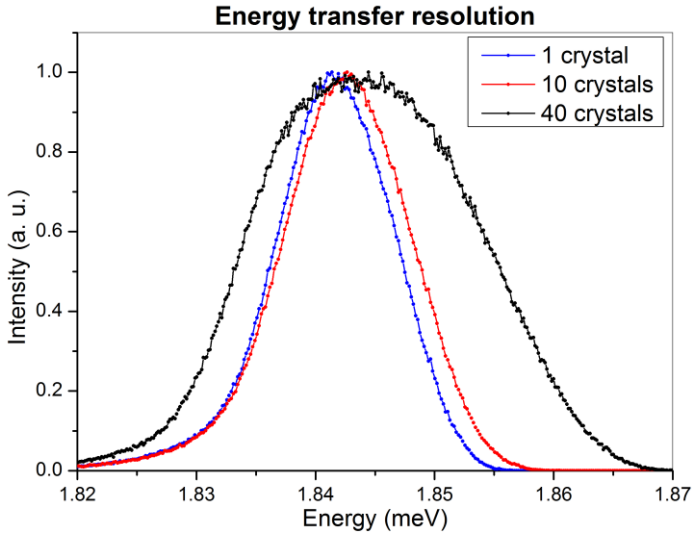

Figure 53: The energy FWHM values are 11.5 μeV for 1 central tile, 12.5 μeV for 10 central tiles and 22.5 μeV for all 40 tiles. The conclusion of this investigation is that the positioning and angular tilt of the OSIRIS crystals plays the biggest role in determining the instrument's energy resolution, as energy resolution becomes significantly bigger with an increase in the number of crystal tiles utilised vertically.

4.6.15. Testing OSIRIS's resolution with a sharp moderator pulse

A short test was performed to understand how the energy resolution of OSIRIS is affected by the moderator time-of-flight spread. The objective was to make the moderator TOF spread very narrow with a use of a pair of choppers inserted just after the moderator. Narrowing down the moderator TOF

FWHM value from around 120 to 10µs eliminates most of the moderator's contribution to the instrument's resolution. The choppers were placed very close to the moderator with the total distance from the moderator to the end of the second chopper remaining below 2 mm. It was possible to achieve the desired cut in moderator TOF through setting very high frequency values for the choppers.

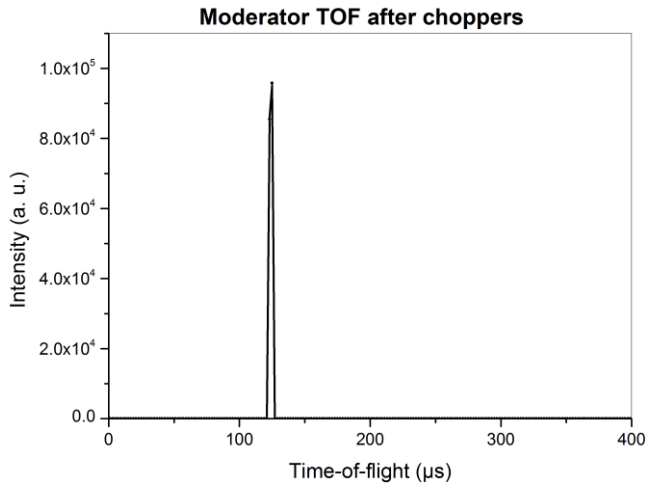

Figure 54: Moderator pulse after most of it has been cut out with the use of choppers.

Setup: SI-2526-364-03-E

Simulated neutron count (narrow pulse setup): 60 billion

As may be observed from this experiment and the graph below, the energy transfer FWHM value decreases by 3% as a result of using narrow moderator pulse. The energy FWHM value is 21.9 µeV for the narrow moderator pulse compared to 22.5 µeV for the full pulse.

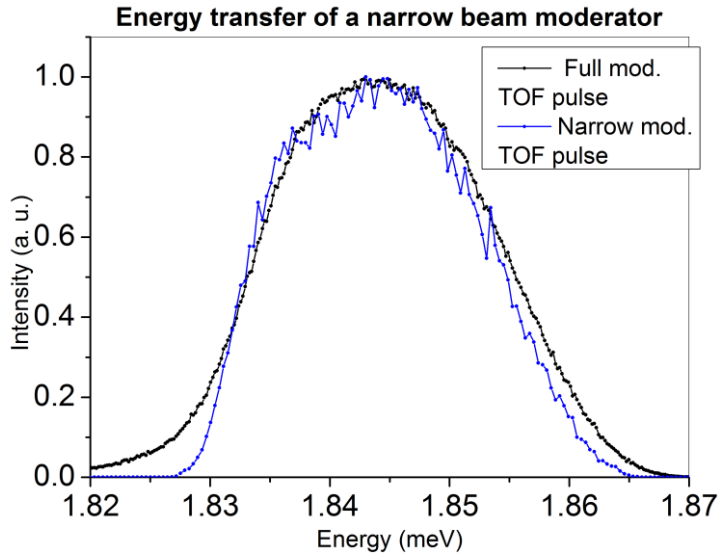

Figure 55: The subtle wing on the left of the energy curve from the full moderator pulse simulation arises from the moderator's TOF distribution which gradually slopes downwards. This leads to an increase in intensity of less energetic neutrons. Note that statistics are poor for the narrow moderator pulse setup due to a lot of neutrons having been absorbed by the choppers in the process.

4.6.16. Comparison of simulated results to experimental data

PG002

In this set of OSIRIS elastic tests the simulated energy and time-of-flight resolution curves were compared to the corresponding experimental curves to see how well the instrument has been modelled. The multiple slab modification shown in the previous section has been removed as it was very experimental and didn't show desirable results. The *4.65° offset setup* was not included as it performs very similar to the original *SI-2526-364-03-E setup*.

The simulated resolution curves were normalised in neutron intensity, but not shifted along the x-axis for the time-of-flight measurements as it is important to judge the performance by time-of-flight arrival as well as curve shape to make sure that the peak values of the simulated results coincide with the experimental data.

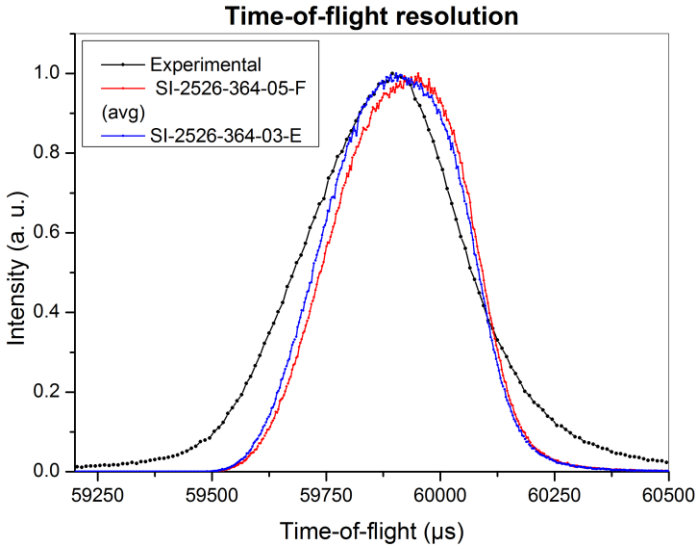

Figure 56: The SI-2526-364-03-E setup produces a larger TOF FWHM value of 364.3μs compare to 356.1μs for the averaged setup. That constitutes to approximately a 3% difference between the two.

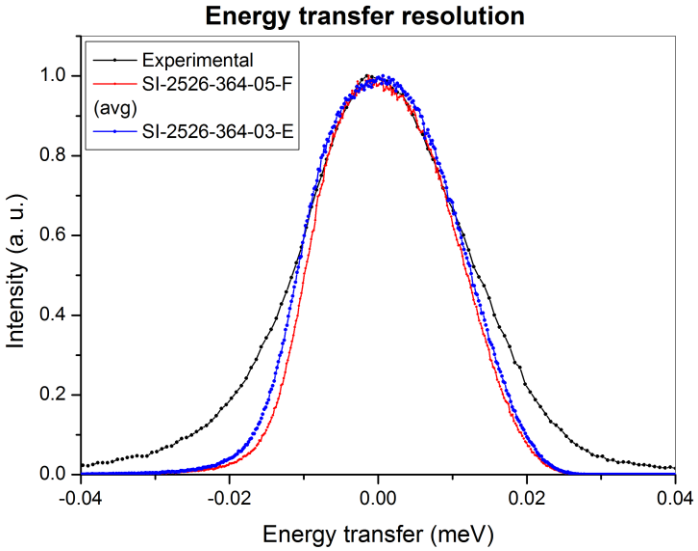

Figure 57: Energy transfer resolutions of the two engineering setups compared to experimental results. The SI-2526-364-03-E setup produces a slightly larger FWHM value of 23.5μeV, compared to 22.0 for the averaged setup. This accounts for approximately a 7% FWHM difference.

PG004

Now the PG004 performance of the *SI-2526-364-03-E* setup is compared to experimental results.

Setup	TOF FWHM (μs)	Energy FWHM (μeV)	Integrated intensity	Neutron count
Experimental	189.4	99.5	N/A	N/A
SI-2526-364-03-E	185.0	95.6	24.8015	9 257 960

Table 11: Comparing performance of the SI-2526-364-03-E setup to experimental data.

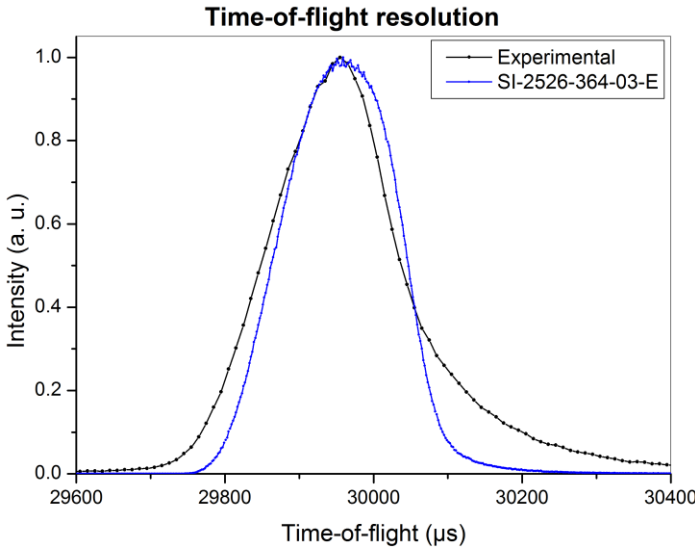

Figure 58: As has been the case previously for the PG002 comparisons, simulated results resemble experimental data closely in FWHM values.

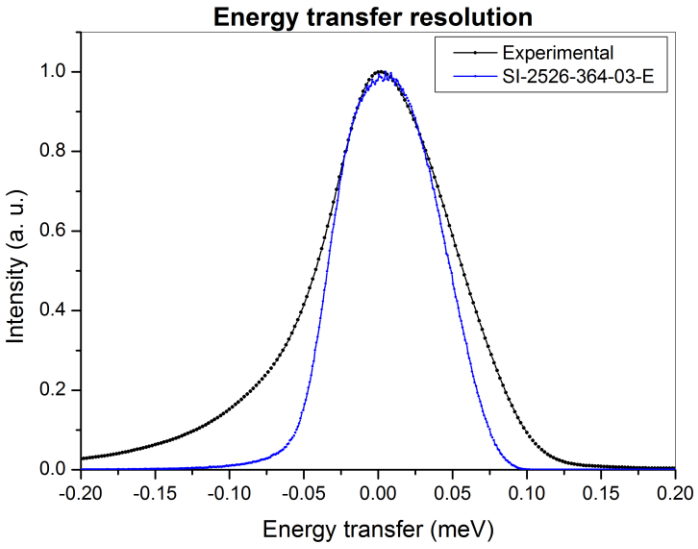

Figure 59: The PG004 energy resolution curves for the experimental data compared to the SI-2526-364-03-E setup.

5. Further investigations

Once OSIRIS was modelled to show good resemblance to the experimental resolution, it was time to investigate further properties of the instrument, most of which are not easily measurable and require evaluation with the use of Monte Carlo methods to allow for a better understanding of the instrument. These investigations can aid greatly by saving time and resource that would otherwise be spent on studying instrument's properties empirically.

5.1. Inelastic scattering resolution of OSIRIS

One such experiment involved simulating the inelastic scattering resolution of OSIRIS as a function of energy transfer. For this purpose the vanadium sample was replaced with a similar, but inelastic incoherent scattering component "tunneling_sample". This component allows for the study of elastic, quasi-elastic and inelastic effects.

As is done on OSIRIS, the mean TOF value of approximately 2 668 μs of the secondary flight path was subtracted from the spectroscopy detector TOF values and converted to energy using the primary OSIRIS flight length of approximately 34 m.

Setup: SI-2526-364-03-E

Simulated neutron count: 1 billion

Tunnelling energy	TOF FWHM (μs)	Energy FWHM (μeV)	Integrated intensity	Neutron count
0.1	339.06	22.71	3.39495	2 811 720
0.2	316.09	22.49	3.28061	2 781 830
0.4	279.46	22.78	3.09502	2 716 370
0.5	263.66	22.60	2.97879	2 333 960
1.0	202.74	22.79	2.63732	2 588 660
1.5	166.38	23.64	2.29335	2 403 540

Table 12: Time-of-flight and energy FWHM values as a function of tunnelling energy.

2.0	140.46	24.48	2.04883	1 988 760
2.5	127.02	25.77	1.81529	2 114 510
3.5	98.72	26.90	1.42387	1 614 090
4.0	92.09	29.03	1.25185	1 531 360
4.5	86.83	28.04	1.09894	1 669 530
5.0	80.40	31.30	0.988426	1 620 860
5.5	75.06	31.88	0.892753	1 571 240
6.0	72.44	33.87	0.813394	1 184 900
6.5	70.07	35.87	0.729848	1 280 230
7.0	67.49	37.10	0.661303	1 232 640
8.0	62.95	40.43	0.547693	1 038 420
8.5	62.00	41.66	0.497195	1 118 020
9.0	60.81	44.40	0.456921	1 094 080
9.5	59.51	45.27	0.415398	1 051 570
10.0	57.29	46.10	0.379376	1 021 850
15.0	48.31	62.27	0.127028	523 666
20.0	45.11	82.29	0.0408531	559 412

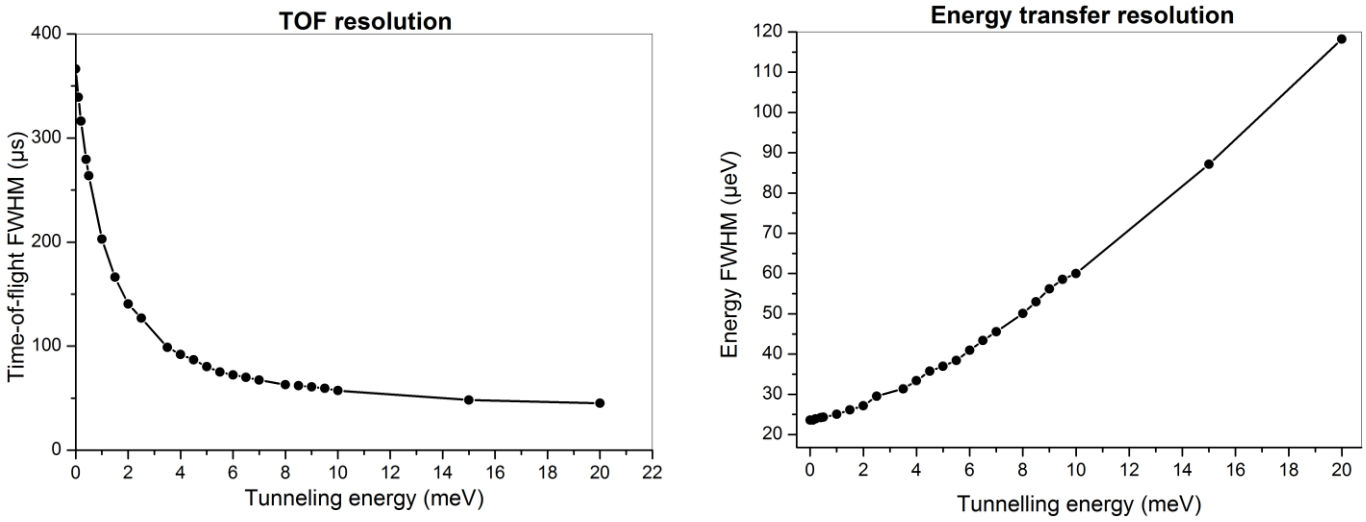

Figure 60: On the left TOF resolution of the instrument. TOF FWHM values decrease with an increase in tunneling energy because neutrons are produced with higher energy at the moderator leading to a narrower TOF distribution. On the right energy resolution of the instrument.

5.2.New moderator tests

In early 2013 new moderator files were developed by Stuart Ansell (ISIS Facility) for ISIS target stations. The files were developed for each of the moderators used across the TS1 and TS2 instruments. A very similar test to 4.1.1 was performed to observe how the new moderator performs in terms of time-of-flight over a range of different wavelengths. Moderator energy was adjusted per each run to achieve the desired wavelength input and the width of the energy input range was kept at 10 µeV each time.

5.2.1. New moderator time-of-flight tests

Wavelength (Å)	Experimental TOF FWHM (µs)
2.2	42
2.6	60
4.4	115
6.3	125
4.05	110

Table 13: A few experimental results obtained for different samples at a number of wavelength values to enable for evaluation of the new moderator.

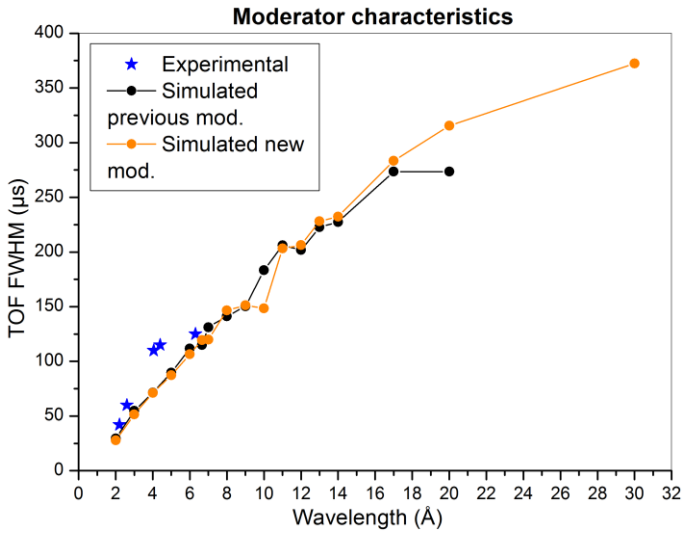

Figure 61: Moderator TOF FWHM values as a function of wavelength. Simulated TOF FWHM values from both moderator files do not agree well with experimental values in the ranges of approximately 3 – 6 Å.

5.2.2. Diffraction moderator comparison

In the subsequent tests both moderators were further compared in two different ways. The first test consisted of comparing the TOF performance of both monitors at 6.28 Å representing the Bragg condition of a silicon sample on OSIRIS. This was done in order to compare simulated moderator TOF FWHM values to experimentally available silicon values. However, this is not a very accurate comparison because of neglecting the OSIRIS's diffraction setup with a flight path of approximately 35 m, which adds to the TOF spread. For this reason a second test was performed with OSIRIS's diffraction spectrometer modelled for silicon diffraction. The energy input range for silicon was kept narrow at 2.0785 - 2.0787 meV to achieve 6.28Å.

Simulated neutron count: 100 million

d-spacing: 3.1367Å

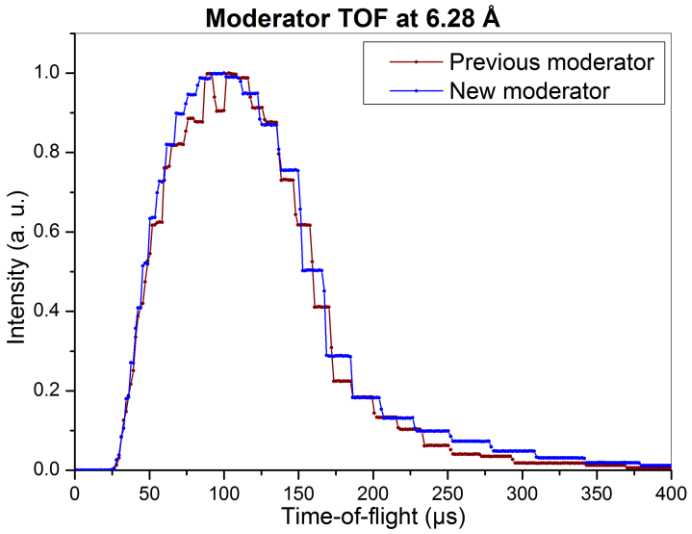

Figure 62: The TOF distribution of the new moderator falls off less steep in intensity at higher TOF values. This is more representative of the real moderator. At 6.28 Å the new moderator has a TOF FWHM value of 120.3 μs and peaks at 100 μs compared to the TOF FWHM value of 111.6 μs and peak intensity at 103.2 μs for the previous moderator.

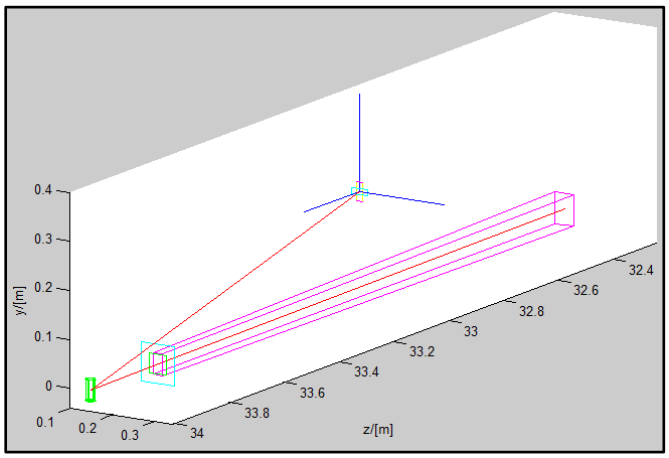

Figure 63: Schematic of the OSIRIS diffraction setup. Distance of the primary spectrometer remains the same 34 m while distance of the secondary spectrometer was set to approximately 1 m. On the figure the diffraction detector is located along the z-axis, behind and above the tapered guide following a backscattering geometry.

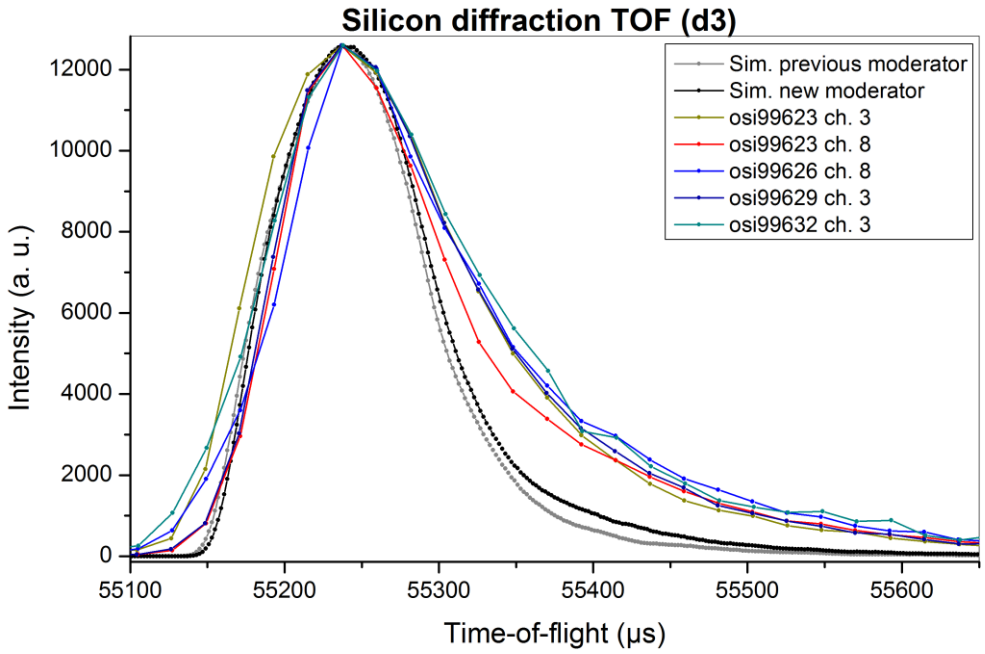

Figure 64: A comparison of silicon diffraction results for both moderators simulated compared to a number of experimental results taken from different diffraction monitors at OSIRIS. The intensity for simulated results was normalised to experimental data. Although the new moderator improves on intensity distribution resulting in a more defined "wing" for less energetic neutrons, it's still relatively far from the experimental results. The TOF FWHM values are 116.3 μs and 118.8 μs using the previous and new moderator files respectively, compared to the experimental value of approximately 145 μs. The experimental value is hence approximately 22% larger than for the new moderator and approximately 25% larger than for the old moderator.

5.2.3. Full OSIRIS simulations with the new moderator

Full simulations of OSIRIS using the new moderator file were run to compare OSIRIS's new resolution with the resolution obtained with the old moderator and experimentally. It may be observed from the figures below that the new moderator file improves the tails of the resolution graphs, more so for the PG004 setup as opposed to PG002 as the moderator tail broadens at higher wavelengths and thus contributes more to the instrument's resolution.

Setup: SI-2526-364-03-E

Simulated neutron count: 1.5 billion

PG002

Setup	TOF FWHM (μs)	Energy FWHM (μeV)	Integrated intensity	Neutron count
Experimental	391.2	25.0	N/A	N/A
Previous moderator	364.3	23.5	8.16304	6 095 860
New moderator	366.0	23.7	4.34276	6 038 100

Table 14: Comparing simulated performance of the two moderator files to experimental data.

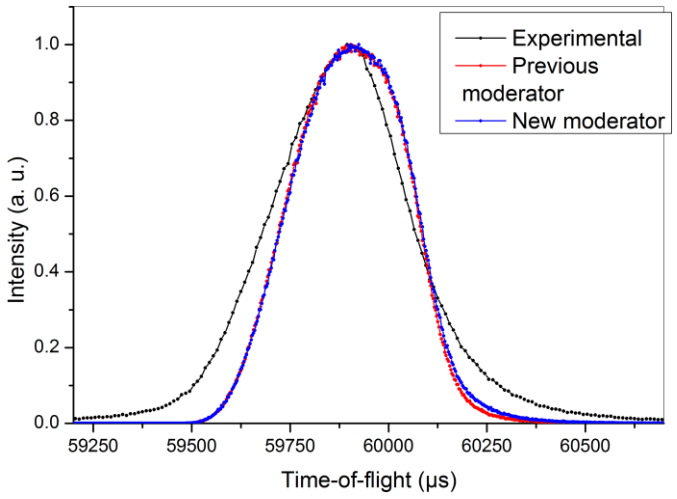

Figure 65: TOF FWHM values are 391.2 μs experimental, 364.3 μs simulated with the previous moderator and 366.0 μs simulated with the new moderator. Both of the moderators perform similarly.

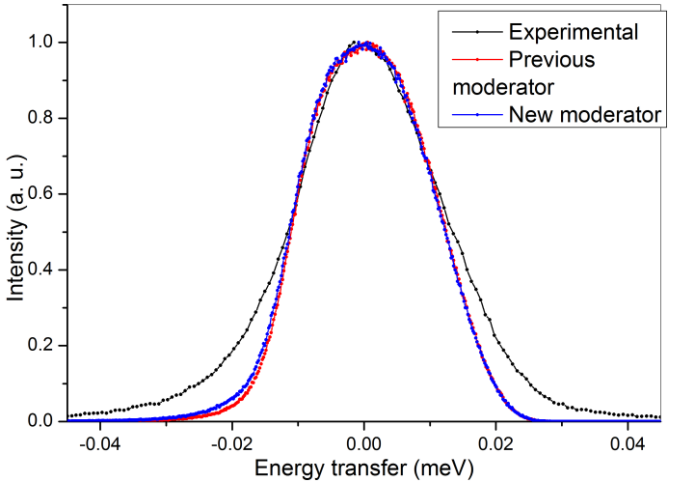

Figure 66: Energy FWHM values are 25.0 μeV experimental, 23.5 μeV simulated with the previous moderator and 23.7μeV simulated with the new moderator.

PG004

Setup	TOF FWHM (μs)	Energy FWHM (μeV)	Integrated intensity	Neutron count
Experimental	189.4	99.5	N/A	N/A
Previous moderator	185.0	95.6	24.8015	9 257 960
New moderator	186.4	96.3	12.7621	9 350 720

Table 15: Comparing simulated performance of the two moderator files to experimental data.

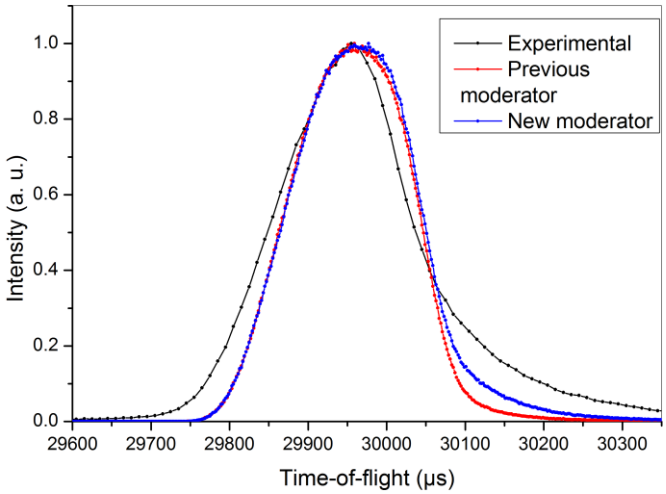

Figure 67: The TOF FWHM values are 189.4μs experimental, 185.0μs for simulated results with the previous moderator and 186.4μs for simulated results with the new moderator. Both of the moderators perform similarly.

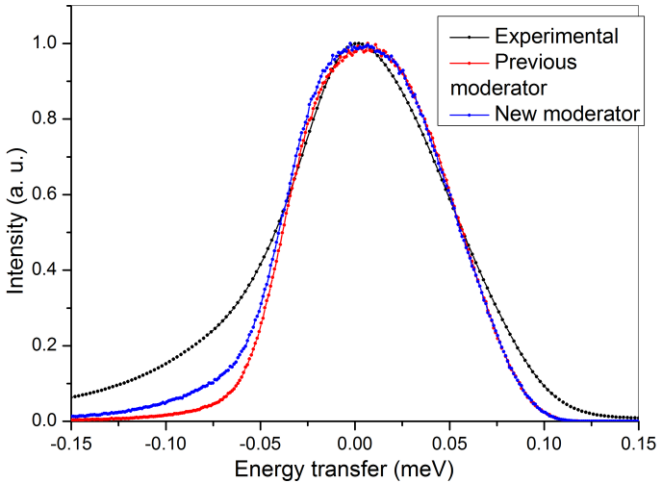

Figure 68: Energy FWHM values are 99.5μeV experimental, 95.6 μeV for simulated results with the previous moderator and 96.3 μeV for simulated results with the new moderator.

5.3.Modelling OSIRIS with the ESS moderator

Finally, a different approach was taken in an attempt to match OSIRIS's experimental resolution curve. For this purpose the hydrogen moderator file was replaced with the versatile "ESS_moderator_short" component file included with McStas. The moderator chosen was the liquid H2, short pulse, decoupled un-poisoned. The resulting simulated resolution of OSIRIS is presented below.

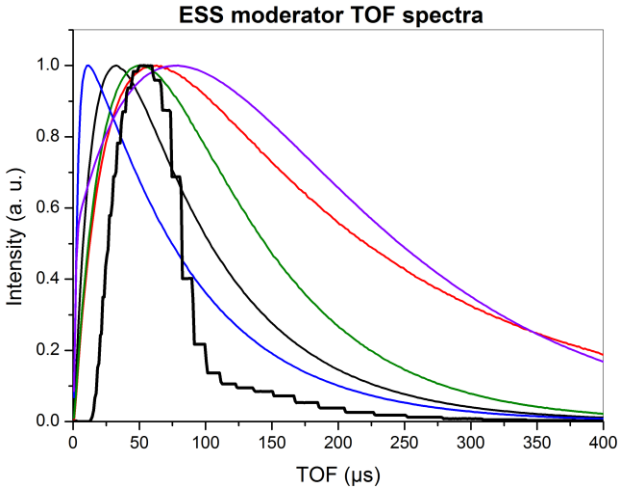

Figure 69: A plot comparing TOF distributions of the ESS moderator with different parameters, compared to the new OSIRIS moderator file seen in black. As may be observed the ESS moderator is quite flexible and with the proper parameters reproduces the missing "wing" of the OSIRIS moderator at lower energies.

Simulated neutron count (ESS): 10 billion

L1=6, L2=7, Freq=50Hz, branchframe=0.5, T=50, tau=1.1 × 10^{-4}, tau1=0. Tau2=1.2 × 10^{-5}, n=1.2, n2=90, chi=0.9, I0=2.7×10^{10}, I2=4.6×10^{10} , branch1=0, branch2=0.5

Setup	TOF FWHM (μs)	Energy FWHM (μeV)
Experimental	391.2	25.0
New moderator	366.0	23.7
ESS moderator	400.0	25.8

Table 16: Comparing the resolution produced with the two moderators to experimental data.

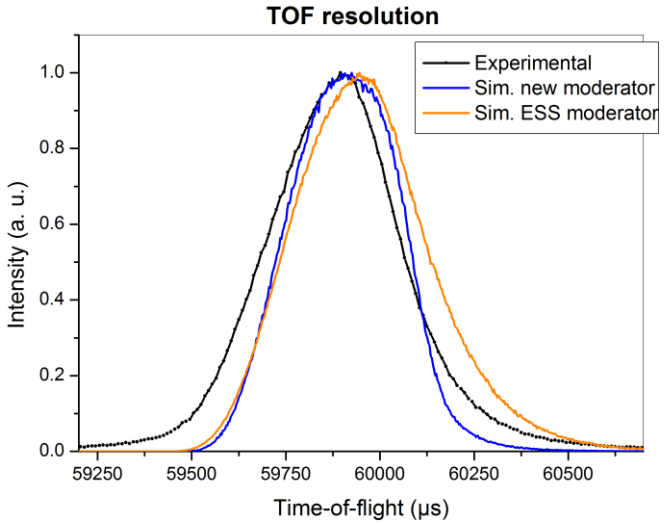

Figure 70: TOF resolutions of OSIRIS. The distribution using the ESS moderator gives larger wings than using the new OSIRIS moderator, and hence matches the experimental TOF resolution better.

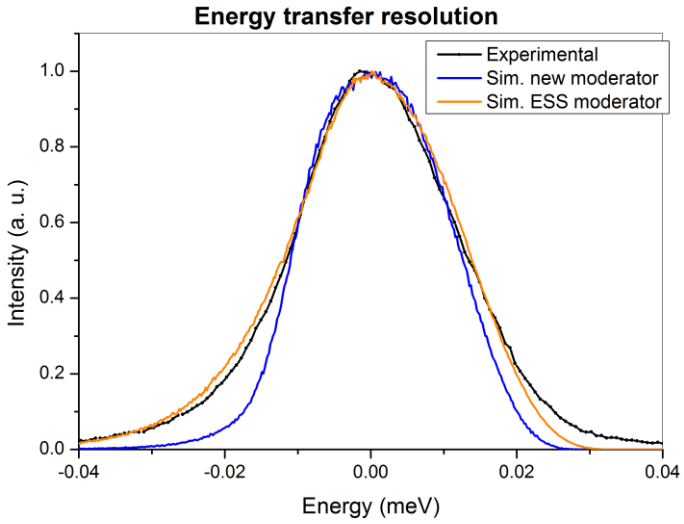

Figure 71: Energy resolution curves of OSIRIS. The energy FWHM values are 25.0 μeV experimental, 23.7 μeV with the new OSIRIS moderator and 25.8 μeV using the ESS moderator.

6. Conclusion

McStas is a neutron ray-tracing software package the basics of which can be picked up quickly if one is interested in gaining better understanding behind the science of neutron spectroscopy as well as statistical computational methods. Due to its own high level meta-language programming environment and automatic compilation of C++ code it requires minimal coding knowledge from the user to begin simulating. The shortcoming of this is a more limited functionality and lack of being able to model more sophisticated physical effects present in software packages like GEANT (**GE**ometry **AN**d **T**racking) used at CERN in Switzerland.

The most problematic component presented in this report was the failure of the "monochromator_pol" component when used in an analyser array. However, other issues were mentioned in the software manual that potentially produce bad statistics, such as the use of various optimisation components, parallel execution with MPI, the use of compiler optimisation flags and others. Few simple precautions had to be taken into account to make sure that using all these options, while benefited in terms of improving simulation speed, did not produce false results. For this purpose many of the optimisation functions were tested and data compared to simulations without them. In some cases, such as when executing the code in MPI, results were found to slightly differ from the non-MPI setup; neutrons passing the guide produced a slightly more asymmetric position distribution with MPI, but this did not affect OSIRIS's simulated resolution in a noticeable way.

Throughout the course of performing hundreds of simulations in order to get a better understanding of how each of the components used in OSIRIS contribute to its resolution it became obvious that the most important factor by far is the analyser geometry. However, modelling Thermal Diffuse Scattering proved to be not possible in McStas. It is not exactly known quantitatively how much TDS contributes to the overall shape of the spectrometer's resolution. As a result OSIRIS's simulated energy resolution FWHM values were slightly lower than experimental. Still, the simulated curves are overall in a good agreement with OSIRIS's experimental data.

Obviously not being able to perfectly match the instruments resolution has its implications on predicting performance of the instrument when modelled under new conditions, such as when testing to find the spectrometer's inelastic resolution or its elastic resolution with a different analyser instead of PG. This adds errors towards simulated results of other properties. The most obvious example is estimating OSIRIS's inelastic resolution as a function of tunnelling energy, where experimental values are not known. McStas is therefore a simple and cost-effective tool that serves the purpose helping instrument scientists get a better insight into the performance as well as study upgrade possibilities of their instruments.

Acknowledgements

I would like to thank Dr Franz Demmel for supervising me on a daily basis whilst I was undertaking this project and providing me with technical assistance. I would like to thank Dr Sergey Saveliev for supervising me on the behalf of Loughborough University. I would also like to thank Dr Felix Fernandez-Alonso for helping me understand the theory behind my work, Dr Stuart Ansell for help on McStas, and Dr Joshaniel Cooper, Roberto S. Pinna (also a placement student) and others who helped me throughout my stay at ISIS by answering many of my questions. Finally I would like to thank ISIS (part of the Rutherford-Appleton Laboratory of STFC) for funding this project and enabling me to gain valuable experience whilst undertaking my industrial placement here.

Bibliography

1. **D.S.Sivia.** The Basics of X-ray and neutron scattering. *Elementary Scattering Theory.* New York : Oxford University Press, 2011, pp. 63-64.

2. *Neutron Scattering Instrumentation.* **H.Schober.** 2009, Neutron Applications in Earth, Energy and Environmental Sciences, Vol. 8.

3. **K.H.Andersen and M.T.F.Telling.** *The OSIRIS User Guide.* Didcot : ISIS Facility, Rutherford Appleton Laboratory, 2005.

4. *A time-of-flight backscattering spectrometer at the Spallation Neutron Source, BASIS.* **E.Mamontov, K.W.Herwig.** 085109, 2011, Review of Scientific Instruments, Vol. 82.

5. *Monte Carlo theory and practice.* **F. James.** Geneva : s.n., 1980, Rep. Prog. Phys, Vol. 43, pp. 1147-1153.

6. **Eric W.Weisstein.** Monte Carlo Integration. *Wolfram Mathworld.* [Online] 2013. [Cited: 22 May 2013.] http://mathworld.wolfram.com/MonteCarloIntegration.html.

7. **P.Willendrup, E.Knudsen, E.Farhi and K.Lefmann.** *User and Programmers Guide to the Neutron Ray-Tracing Package McStas, v 1.12.* Roskilde, Denmark : Risø DTU, 2011.

8. *Spectroscopic characteristics of the OSIRIS near-backscattering crystal analyser spectrometer on the ISIS pulsed neutron source.* **Mark T.F.Telling, Ken H.Andersen.** Phys. Chem. Chem. Phys., 2005, 7, 1255-1261.

9. *The OSIRIS diffractometer and polarisation-analysis backscattering spectrometer.* **K.H.Andersen, D.Martin y Marero, M.J.Barlow.** S237-S239, s.l. : Springer, 2002, Applied Physics A, Vol. 74.

10. **M.T.F.Telling.** *Monte Carlo simulations of the OSIRIS and IRIS neutron spectrometers using the virtual neutron instrumentation tool, VITESS.* Didcot, UK : STFC, 2004.

11. Osiris, High-resolution spectroscopy and diffraction. *Science & Technology Facilities Council.* [Online] STFC, 2013. [Cited: 22 May 2013.] http://www.isis.stfc.ac.uk/instruments/osiris/.

12. *Novel neutron guides.* **P.Allenspach, G.Zsigmond, J.Stahn.** 3-4, 2008, Journal of Neutron Research, Vol. 16, pp. 75-80.

13. **P.K.Willendrup, E.Knudsen, K.Lefmann, E.Farhi.** *Component Manual for the Neutron Ray-Tracing Package McStas, v1.12.* Roskilde, Denmark : Risø DTU, 2011.

Appendices

Appendix 1 – OSIRIS analyser specification

SI-2526-364-03-E		O-SI-2526-364-05-F (averaged)		
Vertical angular tilt (°)	**Distance to sample (m)**	**Vertical angular deviation (°)**	**Distance to sample (m)**	**Assumed horizontal radius of curvature (m)**
18.811	0.866268	18.811	0.865960	0.86596
18.811	0.869616	18.543	0.869257	0.86596
18.397	0.872923	17.747	0.872434	0.86596
16.666	0.875917	16.666	0.875454	0.86596
16.666	0.878738	16.235	0.878371	0.86596
15.925	0.881741	15.162	0.881158	0.86596
14.518	0.884330	14.518	0.883698	0.86596
14.518	0.886909	13.955	0.886332	0.86596
13.512	0.889300	12.887	0.888720	0.86596
12.384	0.891496	12.384	0.890963	0.86596
12.384	0.893678	11.708	0.893099	0.86596
11.125	0.895640	10.643	0.895076	0.86596
10.256	0.897450	10.256	0.896921	0.86596
10.256	0.899245	9.483	0.898663	0.88762
8.829	0.900791	8.413	0.900239	0.88762
8.120	0.902217	8.122	0.901692	0.88762
8.120	0.903628	7.265	0.903044	0.88762
6.530	0.904767	6.196	0.904225	0.88762
5.985	0.905815	5.985	0.905292	0.88762
5.985 (upper central tile)	0.906846	5.058	0.906260	0.88762
4.250 (lower central tile)	0.907586	3.991 (central tile)	0.907052	0.88762
3.855	0.908259	3.855	0.907738	0.88762
3.855	0.908914	2.858	0.908325	0.88762
1.982	0.909258	1.792	0.908731	0.88762
1.726	0.909559	1.726	0.909039	0.88762
1.726	0.909840	0.663	0.909247	0.88762
-0.278	0.909790	-0.4	0.909270	0.88762
-0.400	0.909720	-0.47	0.909194	0.90927
-0.400	0.909626	-1.535	0.909019	0.90927
-2.530	0.909184	-2.53	0.908664	0.90927
-2.530	0.908741	-2.677	0.908209	0.90927
-2.703	0.908249	-3.744	0.907647	0.90927
-4.660	0.907434	-4.66	0.906912	0.90927
-4.660	0.906615	-4.894	0.906076	0.90927
-5.005	0.905721	-5.961	0.905125	0.90927
-6.791	0.904530	-6.791	0.904007	0.90927
-6.791	0.903334	-7.124	0.902786	0.90927
-7.333	0.902031	-8.193	0.901440	0.90927
-8.928	0.900460	-8.928	0.899934	0.90927
-8.928	0.898889	-8.928	0.898363	0.90927

Appendix 2 - 4.65° offset analyser specification

Vertical angular tilt (°)	Distance to sample (m)	Assumed horizontal radius of curvature (m)
19.470	0.865960	0.86596
19.202	0.869257	0.86596
18.406	0.872434	0.86596
17.325	0.875454	0.86596
16.894	0.878371	0.86596
15.821	0.881158	0.86596
15.177	0.883698	0.86596
14.614	0.886332	0.86596
13.546	0.888720	0.86596
13.043	0.890963	0.86596
12.367	0.893099	0.86596
11.302	0.895076	0.86596
10.915	0.896921	0.86596
10.142	0.898663	0.88762
9.072	0.900239	0.88762
8.781	0.901692	0.88762
7.924	0.903044	0.88762
6.855	0.904225	0.88762
6.644	0.905292	0.88762
5.717	0.906.260	0.88762
4.65	0.907052	0.88762
4.514	0.907738	0.88762
3.517	0.908325	0.88762
2.451	0.908731	0.88762
2.385	0.909039	0.88762
1.322	0.909247	0.88762
0.259	0.909270	0.88762
0.189	0.909194	0.90927
-0.876	0.909019	0.90927
-1.871	0.908664	0.90927
-2.018	0.908209	0.90927
-3.085	0.907647	0.90927
-4.001	0.906912	0.90927
-4.235	0.906076	0.90927
-5.302	0.905.125	0.90927
-6.132	0.904007	0.90927
-6.465	0.902786	0.90927
-7.534	0.901440	0.90927
-8.269	0.899934	0.90927
-8.269	0.898363	0.90927

Appendix 3 - Investigating the effect of crystal mosaic spread on the energy resolution

This investigation involved observing how crystal mosaic spread affects final energy resolution of a simple spectrometer. A total of 8 tests were performed, each consisting of 8 parts to test mosaic properties of the "Monochromator_curved" and "Monochromator_pol" components, 4 tests per each component, 8 different mosaic spread values. One aim was to see how energy FWHM values change with increase in mosaic spread of the crystals at analyser tilt angles of 5° and 45° from the initial ray condition, horizontally and vertically, constitution to Bragg conditions of 85° and 67.5° respectively. The crystal distance was fixed at 3m from the guide, and the detector distance at 3m from the crystal. The energy range used was 1 – 2 meV for the 5° setup and 2.5 – 4.5 for the 45° setup. The mosaic spread tested ranged from 2' to 300'. Finally the crystal d-spacing value was set to 3.3427Å.

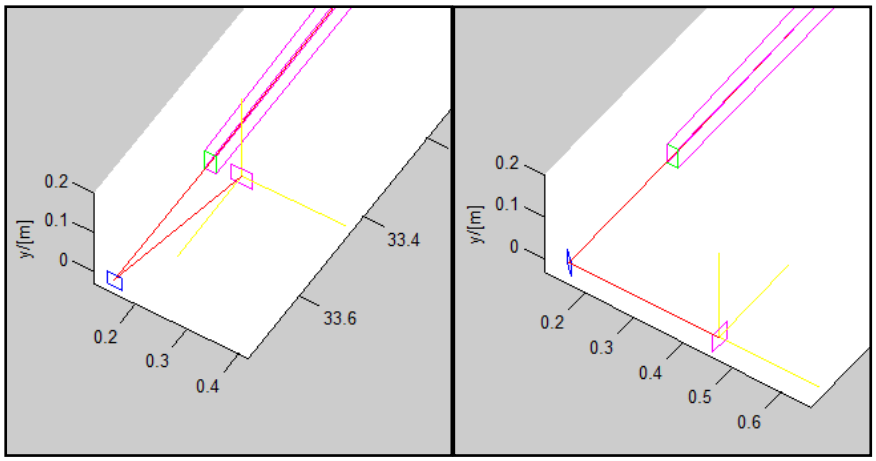

Figure 72: Horizontal setups, 5° and 45° tilt setups respectively showing the guide at the top, the crystal as a blue rectangle and the detector as a purple box.

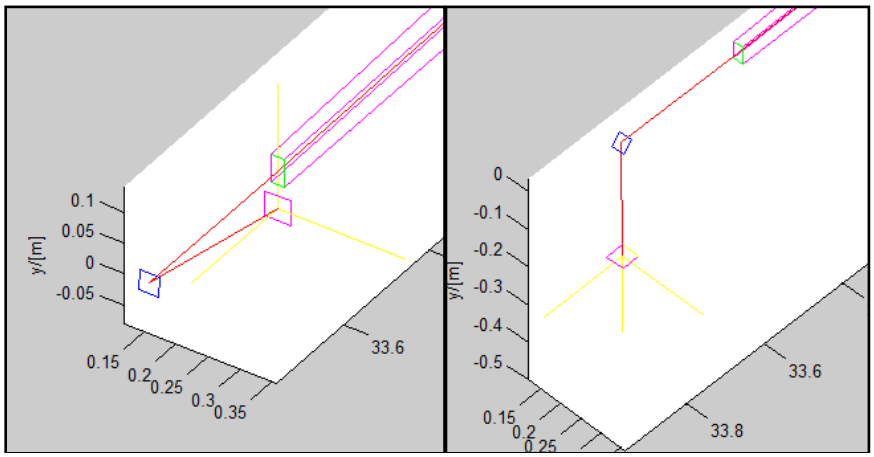

Figure 73: Vertical setups, 5° and 45° tilt setups respectively. Same representation as before.

Simulated neutron count: 500 million

Monochromator_curved

	5° setup			45° setup		
Mosaic spread (')	**Integrated intensity**	**Neutron count**	**E. FWHM (µeV)**	**Integrated intensity**	**Neutron count**	**E. FWHM (µeV)**
2.0	5 350.69	9 540	7.69	84 891	184 638	15.66
44.6	113 109	204 846	15.98	1 864 010	3 975 630	33.22
87.1	200 211	370 446	15.81	3 434 810	7 199 830	33.64
129.7	257 555	489 202	15.81	4 599 690	9 633 620	36.08
172.3	287 701	562 793	16.48	5 309 170	11 248 600	38.24
214.9	295 632	597 048	16.82	5 636 750	12 141 000	40.40
257.4	290 928	607 311	17.16	5 693 510	12 474 500	42.25
300.0	278 482	598 105	17.49	5 587 970	12 421 600	43.48

Table 17: Results for the horizontal detector setup.

	5° setup			45° setup		
Mosaic spread (‘)	**Integrated intensity**	**Neutron count**	**E. FWHM (μeV)**	**Integrated intensity**	**Neutron count**	**E. FWHM (μeV)**
2.0	5 255.75	9 354	10.6	69 337	160 762	17.41
44.6	113 575	203 643	16.84	1 543 780	3 504 740	33.05
87.1	201 715	368 654	16.14	2 873 810	6 409 290	34.06
129.7	259 812	487 985	16.26	3 883 190	8 618 830	35.83
172.3	289 260	561 245	16.82	4 502 930	10074 700	38.6
214.9	296 527	594 748	17.27	4 785 420	10 867 700	40.88
257.4	291 677	603 906	17.61	4 838 950	11 188 800	42.14
300.0	278 034	593 582	18.17	4 755 140	11 183 500	43.65

Table 18: Results for the vertical detector setup.

Monochromator_pol

	5° setup			45° setup		
Mosaic spread (‘)	**Integrated intensity**	**Neutron count**	**E. FWHM (μeV)**	**Integrated intensity**	**Neutron count**	**E. FWHM (μeV)**
2.0	0	0	0	48 465.4	105 177	17.08
44.6	128 113	229 575	15.56	1 896 760	4 119 350	33.42
87.1	255 229	458 701	16.96	3 703 480	8 051 700	34.54
129.7	381 250	683 425	19.77	5 518 850	11 994 400	37.46
172.3	504 923	906 006	23.13	7 329 420	15 933 200	44.63
214.9	628 083	1 127 470	25.38	9 139 400	19 855 200	52.13
257.4	754 696	1 353 540	29.44	10 915 000	23 670 900	59.88
300.0	879 811	1 574 910	33.92	12 626 300	27 335 700	68.11

Table 19: Results for the horizontal detector setup.

	5° setup			45° setup		
Mosaic spread (‘)	**Integrated intensity**	**Neutron count**	**E. FWHM (μeV)**	**Integrated intensity**	**Neutron count**	**E. FWHM (μeV)**
2.0	0	0	0	40 367	93 977	17.68
44.6	0	0	0	1 562 450	3 608 860	33.05
87.1	740.1	2 016	10.29	3 054 770	7 065 170	34.82
129.7	32 880.7	59 174	15.19	4 550 810	10 530 700	39.21
172.3	113 869	200 956	15.53	6 041 440	13 984 700	45.61
214.9	234 870	418 113	16.55	7 528 750	17 409 800	53.05
257.4	439 510	782 870	21.00	8 998 620	20 758 500	59.95
300.0	879 112	1 559 880	33.31	10 401 800	23 927 600	68.67

Table 20: Results for the vertical detector setup.

Results indicate that Monochromator_curved is showing consistent results in both setups, while Monochromator_pol shows a mismatched increase in energy FWHM values between the horizontal and vertical setups. Energy resolution also increases steep for the polarising component with an increase in mosaic spread.

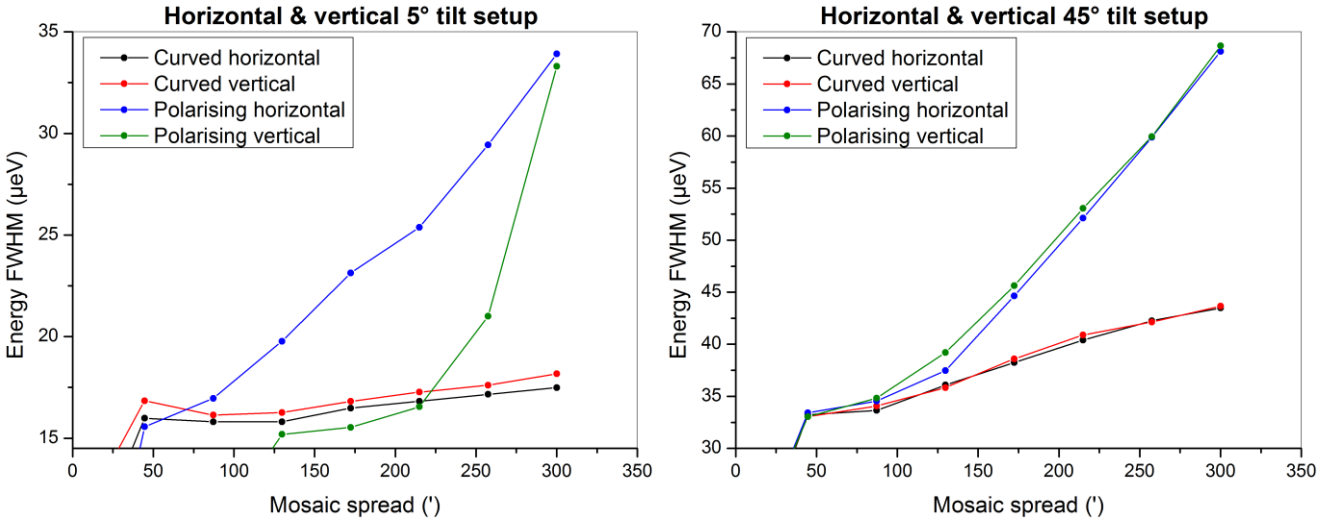

Figure 74: Four curves showing energy FWHM curves at the mosaic spread range of 2' to 300' for the 5° setup on the left, and for the 45° degree setup on the right. The irregular behaviour of the polarising monochromator is observed in both how the vertical and horizontal curves differ for the 5° setup, but also how the Energy FWHM values increase much steeper with an increase in mosaic spread, contrary to the curved monochromator.

Appendix 4 - Evaluating "Virtual_input" and "Virtual_output"

"Virtual_input" and "Virtual_output" are components that serve the purpose of speeding up Monte Carlo simulations by simplifying the instrument simulated. These components work best, for example, when placed at the end of a complex guide made of a lot of individual components, requiring a lot of computational power in order to trace neutrons travelling through it. Virtual_input may be placed at the end of such guide to record all the incoming neutron ray properties from a long simulation into a special file. It is then changed to Virtual_output, which simply reads back recorded data about each individual neutron from the same file, thus outputting same data without spending computational power on tracing those neutrons through the guide.

Simulated neutron count: 100 million

	Time (s)	Neutron count	Neutrons/second
Normal setup	556	1199	2.16
Virtual output	780	2242	2.87

Table 21: Results of a quick benchmark.

Unfortunately this method of optimising simulations didn't prove to be very effective in the case of OSIRIS, most likely because the computational power needed to recall all the parameters about each individual neutrons from the recorded file did not significantly outweigh the computational power required to compute all the neutron paths through the guide. Also, recording a 5 billion neutron simulation with Virtual_input produced a file occupying 28.6 gigabytes in size!

Appendix 5 - Evaluating the "SPLIT" command

The SPLIT command works by artificially repeating events reaching a specific position on the instrument. It relies on a random number generating mechanism inside the component that the code is applied to. The command has the potential to greatly speed up simulations, especially when used on more than one

component at a time. In the case of OSIRIS the most obvious component to use the command on is the sample, which proved to speed up simulations by approximately a factor of 4. The command could also be used on the monochromator components; however, it was found that using the command on too many components at a time lead to problems.

Simulated neutron count: 100 million

Setup	Time taken (s)	Neutron count	Increase factor
Normal	1212	39994	1
With 'split'	3715	403342	3.3

Table 22: A table of results showing data for the 'split' benchmark.

As may be observed from the energy resolution curves presented below the SPLIT command simulates an energy curve identical to the curve using a normal setup. The curve for the SPLIT command does seem be noisier but that's due to higher error from simulating less neutrons.

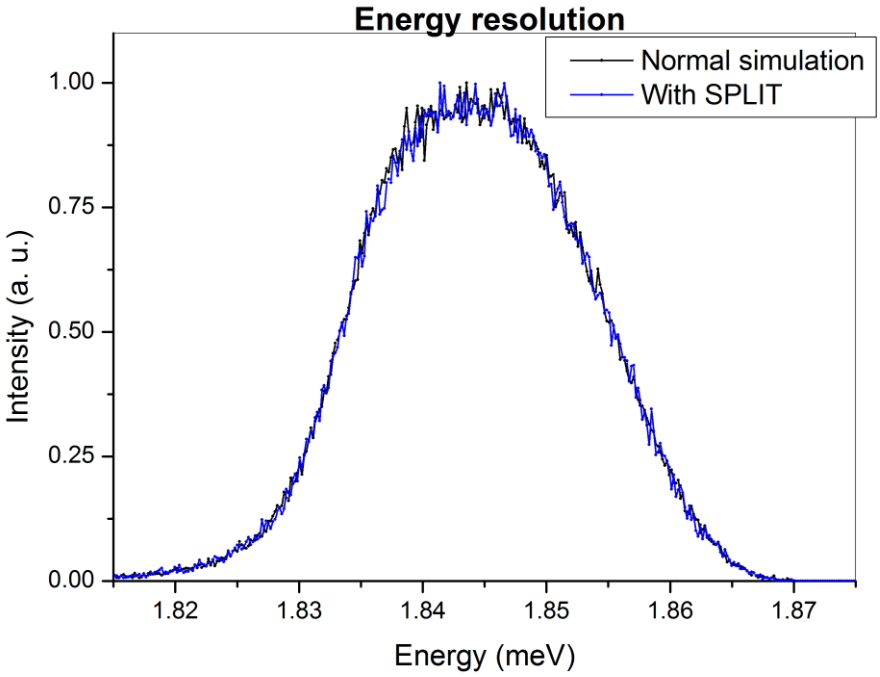

Figure 75: Comparing energy resolution for both setups to ensure reliability of the SPLIT command.

Appendix 6 - Evaluating MPI performance

MPI (**M**essage **P**arsing **I**nterface) is a term that has been coined for parallel execution of computer code on more than one thread. Put simply, in the case of McStas it is the ability of computer software to run a single task on multiple cores of a CPU, or even on multiple CPUs of different architecture. In McStas MPI fits two different scenarios: firstly executing simulations faster on a single PC that has a multi-threaded CPU, thus utilising it to the maximum, and secondly executing a simulation over a grid of computers, were each machine is a separate physical entity, resulting in vast speed improvements. The MPI compiler used in Red Hat was "mpicc".

MPI was tested and used at various points throughout this report to speed up long simulations. The system tested was a PC with an Intel Core i7 (3770k) quad-core processor operating at 3.4GHz with Hyper-Threading technology, thus consisting of a total of 8 threads. The simulations were run under Red Hat Linux 6.3 installed as a guest OS under Windows 7 (using the Oracle VM VirtualBox software). Results are shown in seconds; lower is better. A comparison of the simulations showed a slightly more asymmetric beam distribution at the end of the tapered guide section for the MPI-enabled simulation, compared to the single-threaded simulation. The reason behind this is not exactly known. However, the effect of this on

OSIRIS's resolution curves proved to be negligible, making it indistinguishable from the results obtained without MPI support so the compiler passed the test and no particular bugs were observed throughout using MPI.

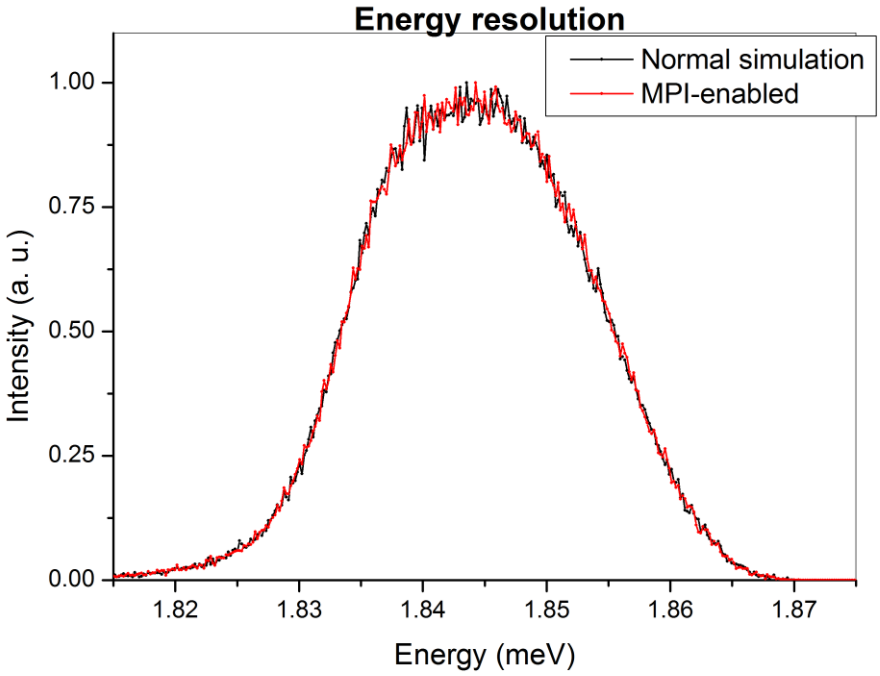

Figure 76: A comparison of OSIRIS's energy resolution curves produced running a regular non-MPI and an MPI-enabled simulations.

	Windows (s)	Red Hat (s)	Relative Red Hat MPI gain	Absolute MPI gain
1 thread	322	415	1.0	0.8
2 threads	N/A	221	1.9	1.5
4 threads	N/A	118	3.5	2.7
6 threads	N/A	105	4.0	3.1
8 threads	N/A	93	4.5	3.5

Table 23: Results of simulations (with Intel TurboBoost disabled to stop dynamic overclocking of the first and second cores when other cores are idle). Note that an Intel i7 CPU is quad-core and uses its "real" cores when loaded up to 4 threads and the additional 4 "virtual" cores on top of that when it's loaded beyond 4 threads. This explains why Red Hat scales almost 4x for the 4-threaded MPI simulation and only 4.5x for the full 8-threaded simulation. Hence McStas scales well in parallel execution, at least on a machine with one physical CPU. The absolute MPI gain compares performance of McStas in Red Hat to Windows. McStas runs slower under Red Hat, as the latter is ran as a guest OS under Windows itself, leading to bigger resource drain.

Appendix 7 - Evaluating McStas data merge tool

The data merge tool supplied with McStas is the part of a toolkit that serves the purpose of converting raw simulation data between different formats as well as merging multiple datasets of the same parameters into a single dataset. When the OSIRIS model became more complex it was thought that this tool could speed up simulations through enabling one to split big simulations into smaller chunks to run on more than one computer at a time, and merging the data from those machines back into one dataset. The figure below compares the energy resolution graph of a 1.5 billion neutron simulation to merged data consisting of three separate simulations, each ran with 0.5 billion neutrons. The merged data neutron count confirms that McStas is able to merge data from the three separate simulations, however, it seems that McStas is unable to correctly calculate the resulting error.

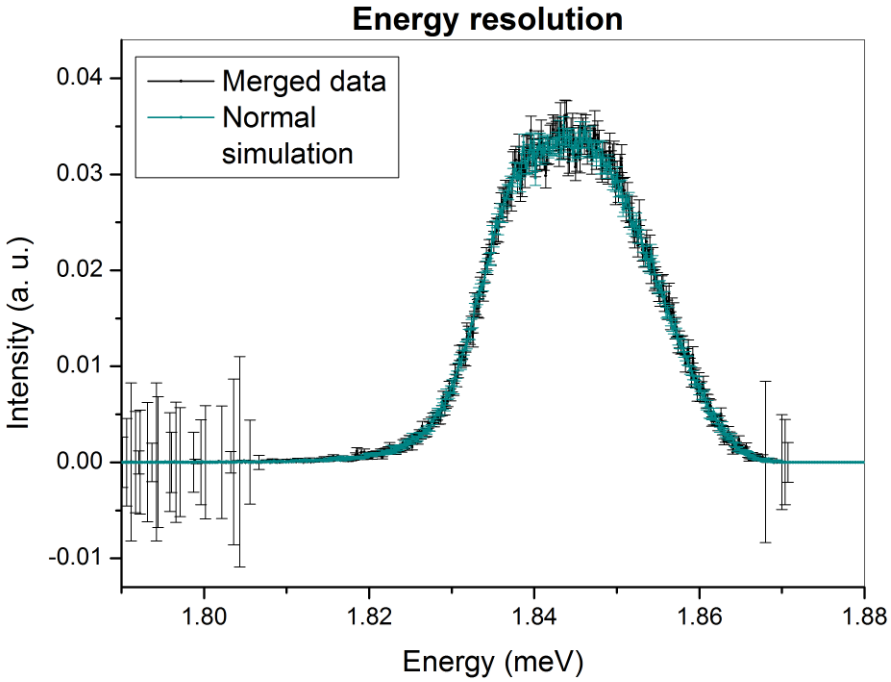

Figure 77: Energy resolution curves for the original 1.5 billion simulation compared to the 3 × 0.5 billion merged simulations.